The Astrophysical Journal, 924:68 (24pp), 2022 January 10 https://doi.org/10.3847/1538-4357/ac4502

Let the Great World Spin: Revealing the Stormy, Turbulent Nature of Young Giant Exoplanet Analogs with the Spitzer Space Telescope

Johanna M. Vos[1], Jacqueline K. Faherty[1], Jonathan Gagné[2,3], Mark Marley[4], Stanimir Metchev[5], John Gizis[6], Emily L. Rice[1,7], and Kelle Cruz[1,8,9]
[1] Department of Astrophysics, American Museum of Natural History, Central Park West at 79th Street, NY 10024, USA; jvos@amnh.org
[2] Planétarium Rio Tinto Alcan, Espace pour la Vie, 4801 av. Pierre-de Coubertin, Montréal, Québec, Canada
[3] Institute for Research on Exoplanets, Université de Montréal, 2900 Boulevard Édouard-Montpetit Montréal, QC Canada H3T 1J4, Canada
[4] University of Arizona Department of Planetary Sciences and Lunar and Planetary Laboratory, USA
[5] Department of Physics & Astronomy and Centre for Planetary Science and Exploration, The University of Western Ontario, London, Ontario N6A 3K7, Canada
[6] Department of Physics and Astronomy, University of Delaware, Newark, DE 19716, USA
[7] Macaulay Honors College, 35 W. 67th Street, New York, NY 10023, USA
[8] Department of Physics and Astronomy, Hunter College, City University of New York, 695 Park Avenue, New York, NY 10065, USA
[9] Flatiron Institute, 162 Fifth Avenue, New York, NY 10010, USA
Received 2021 August 25; revised 2021 November 18; accepted 2021 December 18; published 2022 January 13

Abstract

We present a survey for photometric variability in young, low-mass brown dwarfs with the Spitzer Space Telescope. The 23 objects in our sample show robust signatures of youth and share properties with directly imaged exoplanets. We present three new young objects: 2MASS J03492367+0635078, 2MASS J09512690−8023553, and 2MASS J07180871−6415310. We detect variability in 13 young objects, and find that young brown dwarfs are highly likely to display variability across the L2–T4 spectral type range. In contrast, the field dwarf variability occurrence rate drops for spectral types >L9. We examine the variability amplitudes of young objects and find an enhancement in maximum amplitudes compared to field dwarfs. We speculate that the observed range of amplitudes within a spectral type may be influenced by secondary effects such as viewing inclination and/or rotation period. We combine our new rotation periods with the literature to investigate the effects of mass on angular momentum evolution. While high-mass brown dwarfs ($>30M_{\rm Jup}$) spin up over time, the same trend is not apparent for lower-mass objects ($<30M_{\rm Jup}$), likely due to the small number of measured periods for old, low-mass objects. The rotation periods of companion brown dwarfs and planetary-mass objects are consistent with those of isolated objects with similar ages and masses, suggesting similar angular momentum histories. Within the AB Doradus group, we find a high-variability occurrence rate and evidence for common angular momentum evolution. The results are encouraging for future variability searches in directly imaged exoplanets with facilities such as the James Webb Space Telescope and 30 m telescopes.

Unified Astronomy Thesaurus concepts: Brown dwarfs (185); T dwarfs (1679); L dwarfs (894); Free floating planets (549); Atmospheric variability (2119)

1. Introduction

The atmospheres of brown dwarfs and exoplanets with temperatures <2300 K are characterized by the presence of condensate clouds, which shape their emergent colors and spectra. Based on the handful of directly imaged exoplanets discovered and investigated to date (e.g., β Pictoris b, HR8799bcde, 2M1207b, 51 Eri b; Chauvin et al. 2004; Marois et al. 2008, 2010; Lagrange et al. 2010; Macintosh et al. 2015), it is clear that in-depth investigations of these planets will hinge on a thorough understanding of condensate cloud chemistry and its relationship with surface gravity, temperature, and metallicity.

Time-resolved atmospheric monitoring of brown dwarfs and exoplanets directly probes atmospheric features such as condensate clouds. In the last decade, our understanding of clouds in brown dwarf atmospheres has been revolutionized by a number of infrared studies of rotationally modulated variability. Large surveys (Buenzli et al. 2014; Radigan et al. 2014; Wilson et al. 2014; Metchev et al. 2015; Eriksson et al. 2019) have revealed that variability is common across L and T spectral types (Metchev et al. 2015), with a possible enhancement in variability amplitude and occurrence rate across the L/T transition (Radigan et al. 2014). First results from dwarf monitoring of Y dwarfs with the Spitzer Space Telescope suggest that variability is also common at the lowest temperatures (Cushing et al. 2016; Esplin et al. 2016; Leggett et al. 2016). Multiwavelength characterization studies have provided insight into the vertical atmospheric structure of brown dwarfs and planetary-mass objects, since different wavelengths probe different atmospheric pressures. For example, comparing variability amplitudes at different wavelengths provides information on the types of clouds present (Artigau et al. 2009; Radigan et al. 2012; Apai et al. 2013; Kellogg et al. 2017; Biller et al. 2018), and phase shifts between light curves of different wavelengths have revealed multiple cloud layers (Buenzli et al. 2012; Biller et al. 2013).

Physical mechanisms that can explain observed spectroscopic and photometric variations without clouds have also been proposed. Models presented by Morley et al. (2014) for mid-to-late T dwarfs and Y dwarfs show that hot spots can lead to variability. Tremblin et al. (2020) suggest that variability may be driven by temperature fluctuations that arise as a result of thermochemical instabilities. Moreover, brown dwarfs are

known to exhibit magnetically driven aurorae, which may also drive infrared variations (e.g., Hallinan et al. 2015; Kao et al. 2016; Pineda et al. 2017). Spectroscopic variability monitoring will be necessary to confirm the spectral signatures predicted by each model and to disentangle the effects of each atmospheric process.

Photometric and spectroscopic monitoring is likely to reveal important insights into the atmospheres of directly imaged exoplanets. Indeed, there have already been a number of variability detections in wide-orbit companions with masses in the range $\sim$10–30 $M_{\rm Jup}$ (Zhou et al. 2016, 2018, 2020; Naud et al. 2017). For the closer-in directly imaged exoplanets, there have been two attempts to detect photometric variability in the HR8799 bc planets (Apai et al. 2016; Biller et al. 2021). However, neither study detected variability in the planets, and they placed upper limits of 5%–10% on the variability amplitudes. The James Webb Space Telescope (JWST) will enable unprecedented sensitivity and stability for future variability observations of directly imaged exoplanets such as HR8799 bcde and β Pictoris b.

Young, isolated brown dwarfs are emerging as a bridge population to giant exoplanets. This population is vastly easier to study without the glare of a bright host star, and exist in greater numbers than the current population of known directly imaged exoplanets (Cruz et al. 2009; Allers & Liu 2013; Gagné et al. 2015c; Faherty et al. 2016; Liu et al. 2016). The colors and spectra of this new population are remarkably similar to the directly imaged exoplanets: they exhibit redder near-infrared colors than higher-mass field brown dwarfs with the same spectral type and appear fainter than their equivalent-temperature, more massive counterparts (Faherty et al. 2016; Liu et al. 2016). These differences are generally explained by enhanced atmospheric clouds and/or vertical atmospheric mixing (e.g., Barman et al. 2011; Marley et al. 2012), arising from the lower surface gravity of the younger objects. Since surface gravity appears to have a large effect on the atmospheric and cloud properties of brown dwarfs and directly imaged exoplanets, it follows that variability may be distinct for the low-gravity population.

A number of variability studies have focused on young, low-gravity free-floating and companion objects, and initial studies of young free-floating objects suggest that variability may be enhanced compared to field brown dwarfs. The first detection of cloud-driven variability in a planetary-mass object for the 23 Myr old β Pictoris moving group member PSO J318.5−22 showed the largest variability amplitude to date in an L dwarf (Biller et al. 2015). This initial discovery was followed by a notable sample of low-gravity objects showing high-amplitude variability (Lew et al. 2016; Zhou et al. 2016; Vos et al. 2018; Bowler et al. 2020; Zhou et al. 2020). Metchev et al. (2015) note a potential enhancement in amplitude in a sample of five low-gravity L3-L5.5 brown dwarfs at 3.6 μm and 4.5 μm. Vos et al. (2020) also note an apparent amplitude enhancement for young late-L dwarfs at 4.5 μm based on a compilation of all of the objects monitored with Spitzer to date. Recently, the high-amplitude variables SIMP J0136+09 and 2MASS J2139+02 were identified as members of the $\sim$200 Myr old Carina-Near moving group (Gagné et al. 2017; Zhang et al. 2021). There is also evidence for a higher variability occurrence rate in young brown dwarfs. Vos et al. (2019) carried out a large, ground-based survey for J-band variability in isolated low-gravity dwarfs, finding that the young population has a variability occurrence rate of 30^{+16}_{-8}%, compared to 11^{+11}_{-4}% of field dwarfs. It is clear that a large, unbiased survey for variability in young, low-gravity objects is necessary to test the tentative amplitude and occurrence rate enhancements reported to date.

In this paper, we present the first large survey for variability in young, low-gravity brown dwarfs in the mid-infrared, and the most sensitive survey to date at any wavelength. We describe the sample in Section 2, including the discovery of three new brown dwarfs with evidence of youth in Section 2.1. We describe the Spitzer observations, data reduction, and light-curve analysis in Sections 3 and 4. We discuss the youth and variability properties of each target in detail in Section 5. We discuss the variability occurrence rate of young brown dwarfs in comparison with field brown dwarfs in Section 6, and the variability amplitudes in Section 7. We put the rotation rates of our young sample in context with literature data in Section 8, and specifically discuss the variability properties of AB Doradus members in Section 9. Finally, we lay out some lessons for variability searches in directly imaged exoplanets in Section 10. We summarize our results in Section 11.

2. An Age-calibrated Sample of Exoplanet Analogs

We designed our survey to test the variability properties of young, low-gravity brown dwarfs by comparing our results to the field brown dwarfs observed by Metchev et al. (2015). The similar sample size, observing strategy, and magnitudes of our sample and the Metchev et al. (2015) sample allow us to robustly compare variability properties between them. We present our sample, spectral types, and magnitudes in Table 1, and show our sample in a color–magnitude diagram in Figure 1. Our sample spans spectral types L2—T5, and the L dwarfs in the sample appear redder than the field L-dwarf sequence, which is often a signature of their low gravity.

2.1. Three New Brown Dwarfs with Evidence of Youth from the BASS Ultracool Survey

We present the discovery of three brown dwarfs that display evidence of youth: 2MASS J03492367+0635078, 2MASS J07180871−6415310, and 2MASS J09512690 −8023553. All three objects were discovered as candidate young objects through the BASS-Ultracool survey (J. Gagné et al. 2021, in preparation) based on their kinematics, which are presented in Table 2 and discussed in detail in Section 5. Here, we present their near-IR FIRE/Prism spectra and investigate their spectral signatures of youth.

2.1.1. FIRE/Prism Spectra: Observations and Analysis

We used the FIRE (Simcoe et al. 2013) spectrograph on the 6.5 m Baade Magellan telescope to obtain near-infrared spectra of the three targets to investigate their spectral properties. Observations were taken on 2018 February 01, 2015 November 24, and 2016 January 22 for 2MASS J0349+0635, 2MASS J0718−6415, and 2MASS J0951−8023, respectively, using prism longslit mode, using ABBA nods in each case. Quartz lamps, ThAr lamps, and telluric standards were taken either before our after each target. Airmass ranged from 1.2–1.6 for the three observing sequences. All FIRE/Prism data were reduced and combined using a modified version of the FireHose package as described in Gagné et al. (2015b). We show the $R\sim400$ FIRE/prism spectra of these three targets in Figure 2.

Table 1
The Survey Consists of 26 Brown Dwarfs with Spectral and/or Kinematic Evidence of Youth

Target Name	Spt Opt	SpT IR	Refs	J_{2MASS}	K_{2MASS}	$(J-K)$	[3.6] mag[a]
2MASS J00011217+1535355	⋯	L4β	1	15.46	13.62	1.84	12.613 ± 0.004
2MASS J0030300−145033	L7	L4–L6β	2, 3	16.28	14.48	1.80	13.365 ± 0.008
2MASS J00310928+5749364	⋯	L9	4	14.95	13.22	1.74	11.956 ± 0.003
2MASS J01531463−6744181	L2	L3β	3,6	16.41	14.42	1.99	13.349 ± 0.005
2MASS J03264225−2102057	L5β	L5 β/γ	1,3	16.13	13.92	2.208	12.559 ± 0.003
2MASS J0342162−681732	L4γ	⋯	1	16.854	14.541	2.313	13.579 ± 0.006
2MASS J03492367+0635078	⋯	L5γ	TW	16.742	15.077	1.665	14.181 ± 0.007
2MASS J03552337+1133437	L5γ	L3–L6γ	3, 5	14.05	11.526	2.524	10.339 ± 0.002
2MASS J04473039−1216155	⋯	T2	7	16.48	15.55	0.93	11.868 ± 0.002
2MASS J04590034−2853396	⋯	L7	8	17.429	15.318	2.111	13.924 ± 0.006
2MASS J05065012+5236338	⋯	T4.5	7	15.75	15.6	0.15	14.251 ± 0.008
2MASS J06420559+4101599	⋯	L9	7	16.164	14.28	1.884	12.888 ± 0.013
2MASS J07180871−6415310	⋯	T5	TW	16.62	16.69	−0.07	15.440 ± 0.017
2MASS J08095903+4434216	⋯	L6 pec	1	16.44	14.42	2.02	13.015 ± 0.006
2MASS J09512690−8023553	⋯	L5 pec	TW	17.098	15.28	1.82	14.554 ± 0.008
2MASS J15515237+0941148	L4γ	>L5γ	3	16.32	14.31	2.009	13.243 ± 0.004
2MASS J16471580+5632057	L7	L9 pec(red)	9	16.59	14.48	2.107	13.180 ± 0.005
2MASS J17410280−4642218	⋯	L6-L8γ	3, 10	15.78	13.44	2.34	11.936 ± 0.003
2MASS J20025073−0521524	L5β	L5-7γ	3	15.32	13.42	1.90	12.161 ± 0.002
2MASS J21171431−2940034	⋯	T0	7	15.6	14.15	1.45	13.014 ± 0.004
2MASS J21543454−1055308	L4β	L5γ	1,3	16.44	14.12	2.24	12.979 ± 0.004
2MASS J22062520+3301144	⋯	T1.5	7	16.58	15.75	0.83	14.630 ± 0.011
2MASS J2206450−421721	L4γ	L4γ	3	15.56	13.61	1.95	12.539 ± 0.003
WISE J221628.62+195248.1	⋯	T3	7	16.59	16.28	0.31	14.182 ± 0.007
2MASS J23225299−6151275	L2γ	L3γ	1,5	15.54	13.86	1.68	12.893 ± 0.003
2MASS J23433470−3646021	⋯	L3–L6γ	1	16.57	14.19	2.38	12.835 ± 0.004

Notes. a: 3.6 μm magnitudes were calculated using a two-pixel aperture and applying aperture corrections as detailed in the Spitzer calibration documentation. The quoted magnitude is the mean magnitude, and the error is the standard deviation of the corrected light curve, and thus includes both noise and astrophysical variability.
References. (1) Gagné et al. 2015c; (2) Kirkpatrick et al. 2000; (3) Faherty et al. 2016; (4) Best et al. 2013; (5) Cruz et al. 2009; (6) Reid et al. 2008; (7) Best et al. 2015; (8) Schneider et al. 2017; (9) Kirkpatrick et al. 2011; (10) Schneider et al. 2014; (TW) This work.

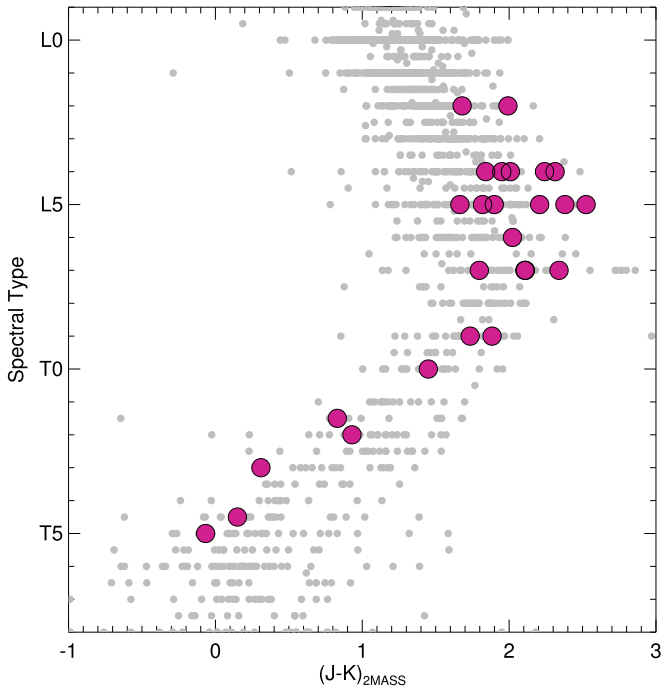

Figure 1. Spectral type—color diagram of our sample of young, low-gravity brown dwarfs (large pink circles) compared to the field population (small gray circles). Our Spitzer sample consists of 26 L3–T5 brown dwarfs with evidence of youth and/or low gravity. The L dwarfs appear redder than the field L-dwarf sequence, which is a signature of their low surface gravity. The field brown dwarf population is drawn from Best et al. (2020).

2.1.2. FIRE/Prism Spectra: Signatures of Youth

We perform a visual spectral classification on each of our new discoveries and an index-based classification on 2MASS J0349+0635 and 2MASS J0951−8023, to assess the evidence of youth and low gravity by comparing our L-type spectra to spectral standard templates reported by Cruz et al. (2018) and our T-type spectrum to known T-type spectral standards.

Based on a visual classification of our FIRE/Prism spectrum of 2MASS J0349+0635, we find that it is matched best by an L5γ spectrum. Using the Allers & Liu (2013) indices, we find that the spectrum is classified as an L4 VL-G. Thus, the spectrum provides strong evidence of youth.

We assign 2MASS J0951−8023 a visual classification of L5 (pec). The spectrum is not well-matched by the spectral type templates, particularly in the *H* band, where there is a "bump" at ∼1.6 μm that is not shown in the L5 templates. The Allers & Liu (2013) index-based classification assigns an L1.6 INT-G spectral type. The disparity between the two spectral types suggests that the peculiarity of the spectrum prohibits a robust spectral classification. If we force the Allers & Liu (2013) classification method to use an L5 spectral type, the gravity classification is INT-G.

Visually, 2MASS J0718−6415 is best-matched by a T5 spectral type. It is very red, emitting a higher flux in *K*-band compared to the T5 template. Interestingly, the spectrum of the planetary-mass AB Doradus member SDSS J111010.01+011613.1 (Gagné et al. 2015a) provides an excellent fit to our spectrum. With a spectral type of T5, we cannot perform

Table 2
Kinematic Information for Sample

Name	μ_α mas yr^{-1}	μ_δ mas yr^{-1}	Ref	RV km s^{-1}	Ref	Parallax mas	Ref	BANYAN Σ	Membership
2MASS J00011217+1535355	143.5 ± 4.5	−174.7 ± 2.4	1	⋯	⋯	31.6 ± 1.8	1	92% ABDMG	HLM ABDMG
2MASS J0030300−145033	256.1 ± 3.4	−41.7 ± 3.3	2[b]	⋯	⋯	41.1 ± 5.3	2	93% ARG	HLM ARG
2MASS J00310928+5749364	522.5 ± 3.5	−23.9 ± 4.0	3	⋯	⋯	71 ± 5	2	96% CARN	HLM CARN
2MASS J01531463−6744181	82 ± 2.7	−21.3 ± 9.4	4	⋯	⋯	⋯	⋯	89% THA	CAN THA
2MASS J03264225−2102057	108.0 ± 5.0	−156.6 ± 4.5	5	⋯	⋯	⋯	⋯	92% ABDMG	HLM ABDMG
2MASS J0342162−681732	73.7 ± 2.3	20.6 ± 7.8	4	⋯	⋯	⋯	⋯	93% THA	HLM THA
2MASS J03492367+0635078	52.0 ± 10.7	−81.9 ± 10.3	5	13.8 ± 3.3	8	⋯	⋯	55% BPMG, 20% ABDMG	AM
2MASS J03552337+1133437	219.8 ± 1.6	−631.3 ± 0.8	1	11.92 ± 0.22	9	109.6 ± 0.7	1	100% ABDMG	BF ABDMG
2MASS J04473039−1216155	−6.3 ± 2.6	−99.1 ± 2.3	2	⋯	⋯	23.0 ± 3.9	2	99% FLD	FLD
2MASS J04590034−2853396	53.8 ± 7.0	84.9 ± 7.2	5	23.4 ± 3.8	8	⋯	⋯.	98% ARG	HLM ARG
2MASS J05065012+5236338	49.8 ± 3.3	−205.9 ± 3.8	2	⋯	⋯	59.6 ± 5.4	⋯	69% FLD	FLD
2MASS J06420559+4101599	−2.0 ± 1.2	−383.1 ± 1.2	7	⋯	⋯	62.6 ± 3.1	7	86% ABDMG	CAN ABDMG
2MASS J07180871−6415310	−175.4 ± 13.5	254.81 ± 13.9	5	13 ± 2	8	⋯	⋯	85% BPMG	CAN BPMG
2MASS J08095903+4434216	−181.9 ± 5.1	− 219 ± 5.1	5	⋯	⋯	42.4 ± 3.6	11	89% FLD	YNG-FLD
2MASS J09512690−8023553	−92.3 ± 9.9	36.8 ± 9.2	5	2.8 ± 3.3	8	⋯	⋯	87% ARG	CAN ARG
2MASS J15515237+0941148	−62.1 ± 0.6	−57.7 ± 0.6	6	−15.2 ± 1.1	8	22.1 ± 1.5	6	100% FLD	YNG-FLD
2MASS J16471580+5632057	−84.6 ± 1.4	241.0 ± 2.6	2	⋯	⋯	42.7 ± 2.1	2	66% FLD	YNG-FLD
2MASS J17410280−4642218	−29.2 ± 2.1	−356.5 ± 2.1	7	−0.9 ± 3.2	8	50.5 ± 2.9	7	99% ABDMG	BF ABDMG
2MASS J20025073−0521524	−111.4 ± 3.1	−114.7 ± 2.4	1	⋯	⋯	56.7 ± 1.5	1	100% FLD	YNG-FLD
2MASS J21171431−2940034	139.3 ± 4.5	− 171 ± 4.8	2	⋯	⋯	52.4 ± 6.8	2	98% BPMG	AM[a]
	149 ± 2.7	−168.1 ± 3.2	7	⋯	⋯	76.1 ± 3.5	7	99% FIELD	AM[a]
2MASS J21543454−1055308	174.9 ± 6.2	−3.3 ± 6.1	5	−20.7 ± 1.0	8	32.6 ± 1	6	80% CARN	CAN CARN
2MASS J22062520+3301144	176 ± 9	16 ± 11	3	⋯	⋯	⋯	⋯	68% ARG	CAN ARG
2MASS J2206450−421721	130.8 ± 1.8	−183.2 ± 2.3	1	⋯	⋯	33.8 ± 1.8	1	99% ABDMG	HLM ABDMG
WISE J221628.62+195248.1	160.4 ± 14.8	−71.53 ± 15.0	5	⋯	⋯	⋯	⋯	85% BPMG	CAN BPMG
2MASS J23225299−6151275	80.1 ± 1.4	−82.0 ± 1.6	1	6.8 ± 0.8	10	23.2 ± 1.0	1	99% THA	BF THA
2MASS J23433470−3646021	124.5 ± 5.5	−105.7 ± 4.7	5	⋯	⋯	⋯	⋯	75% ABDMG	CAN ABDMG

Notes. BF: Bona fide member, HLM: High-likelihood member, CAN: Candidate member, FLD: Field member
[a] We classify 2MASS J21171431−2940034 as ambiguous because Best et al. (2020) and Kirkpatrick et al. (2021) present discrepant parallax values for this target.
[b] The radial velocities quoted from J. Gagné et al. (2021, in preparation) are determined following the method presented in Gagné et al. (2017, 2018a).
References (1) Gaia Collaboration et al. 2018; (2) Best et al. 2020; (3) Best et al. 2015; (4) Gagné et al. 2015b; (5) Marocco et al. 2021; (6) Liu et al. 2016; (7) Kirkpatrick et al. 2021; (8) J. Gagné et al. 2021, in preparation; (9) Blake et al. 2010; (10) Faherty et al. 2016; (11) Faherty et al. 2012.

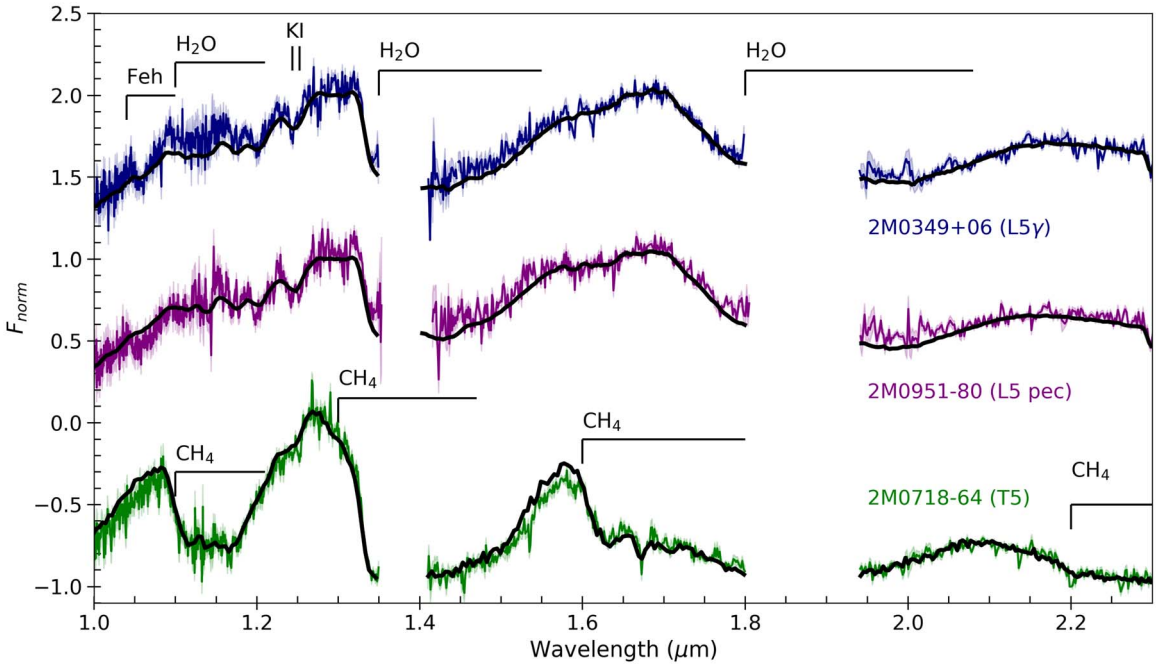

Figure 2. FIRE/Prism spectra of three new young brown dwarfs presented in this paper: 2MASS J0349+0635 (L5γ), 2MASS J0718−6415 (T5), and 2MASS J0951−8023 (L5 (pec)). Spectral templates for an L5γ, an L5, and a T5 are overplotted in black. The spectral resolution ranges from 500 at *J* to 300 at *K*. These objects were discovered and classified as young as part of the BASS-Ultracool survey (J. Gagné et al. 2021, in preparation).

the index-based classification of Allers & Liu (2013) on this target.

2.2. YMG Membership Probabilities of the Sample

For each target in our sample, we assess the likelihood of kinematic membership in nearby young moving groups. Proper motions, radial velocities, and parallaxes used in our kinematic analysis are shown in Table 2. We use these as inputs for the BANYAN Σ tool (Gagné et al. 2018b), which assesses the probability that a source is a member of a young moving group based on its observed kinematics. We additionally use the LACEwING tool (Riedel et al. 2017) to check for consistency, but for clarity we only present the BANYAN Σ results. We consider the following moving groups: TW Hydra (TWA, 10 ± 3 Myr; Bell et al. 2015), β Pictoris (β Pic, 22 ± 6 Myr; Shkolnik et al. 2017), Columba (COL, 42^{+6}_{-4} Myr; Bell et al. 2015), Tucana-Horologium (THA, 45 ± 4 Myr; Bell et al. 2015), Carina (CAR, 45 ± 4 Myr; Bell et al. 2015), Argus (ARG, 30–50 Myr; Torres et al. 2008), AB Doradus (ABDMG, 110–150 Myr; Luhman et al. 2007; Barenfeld et al. 2013), and Carina-Near (CARN, 200 ± 50 Myr; Zuckerman et al. 2006). Field objects are estimated to have ages >1 Gyr. We show the kinematic information and results from membership tools in Table 2. We use the BANYAN Σ results to make a final assessment on each target using the following categories:

1. Bona fide member (BF): an object with full kinematic information (parallax, proper motion, and radial velocity), membership probability >90%, and spectroscopic signs of youth.
2. High-likelihood member (HLM): An object with membership probability >90%, but lacking full kinematic information.
3. Candidate member (CAN): An object that shows greater probability of moving group membership than being a field object, with missing kinematic information.
4. Field object (FLD): An object that is kinematically eliminated from falling into a known nearby moving group based on current kinematic information, or if the spectrum looks unambiguously field age.
5. Young field object (YNG-FLD): An object that is kinematically eliminated from falling into a known nearby moving group based on current kinematic information, but other observational features point to its youth.
6. Ambiguous object (AM): An object that requires updated astrometric precision because it could either belong to more than one group or it cannot be differentiated from the field.

As shown in Table 2, our sample is composed of three bona fide members (2MASS J0355+1133, 2MASS J1741−4642, and 2MASS J2322−6151), seven high-likelihood members, eight candidate members, two field objects, four young field objects, and two ambiguous members. We discuss the kinematic and spectral indicators of youth for each object in detail in Section 5. In Figure 3, we plot the full sample on a color–magnitude diagram.

3. Spitzer Observations and Data Reduction

We used the Infrared Array Camera (IRAC; Fazio et al. 2004) to observe our targets in the Channel 1 (3.6 μm) band as part of the Cycle 14 Program: "The Young and the Restless: Revealing the Turbulent, Cloudy Nature of Young Brown Dwarfs and Exoplanets" (PID: 14128, PI: J Faherty). The observations were designed following the recommendations for obtaining high-precision photometry from the Spitzer Science Center, and following the many examples of brown dwarf variability monitoring in the literature (Metchev et al. 2015;

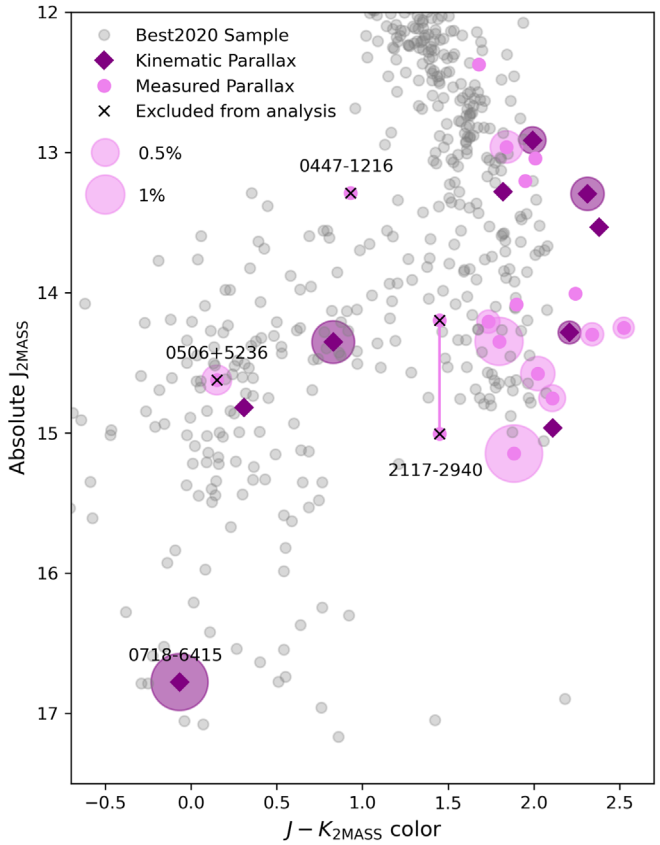

Figure 3. Spitzer variability sample shown in a color–magnitude diagram for objects with measured parallaxes (pink circles) and kinematic parallaxes (purple diamonds), compared to the larger population of brown dwarfs. For sources identified as significantly variable in Section 4, their amplitudes are proportional to the partially transparent symbol size. For reference, 0.5% and 1% variability amplitudes are shown in the top left. We exclude three sources, which are denoted by black crosses, from our variability analysis: 2MASS J0506+5236 and 2MASS J0447−1216 have kinematics that are consistent with field membership, and 2MASS J2117−2940 has highly discrepant parallax measurements. Most members of the sample fall into their expected positions relative to the field brown dwarf sample. 2MASS J0447−1216 is overluminous compared to other field brown dwarfs, possibly due to unresolved binarity. The T5 dwarf 2MASS J0718−6415 is the faintest and coldest object in the sample.

Apai et al. 2017; Biller et al. 2018; Vos et al. 2018, 2020; Allers et al. 2020; Zhou et al. 2020). Science images were obtained in staring mode, using 12 s exposures for a total monitoring duration of 20 hr. Science observations were preceded by a 30-minute dithered sequence to remove the initial slew settling that occurs when acquiring a new target, and followed by a 10-minute dithered sequence to capture the most accurate dark image for each observation.

We follow the same data reduction outlined in Vos et al. (2020); we measured photometry from the Basic Calibrated Data (BCD) images produced by the Spitzer Science Center using pipeline version S19.2. The BOX_CENTROIDER.PRO routine was used to find the centroids of the target and reference stars of similar brightness in the field of view. Aperture photometry was performed on the target and reference stars using apertures with radii of 2.0–5.0 pixels, in steps of 0.25. We choose the final aperture size that produces the lowest rms target light curve. Outliers were identified and rejected from the raw light curves using a 6σ clip.

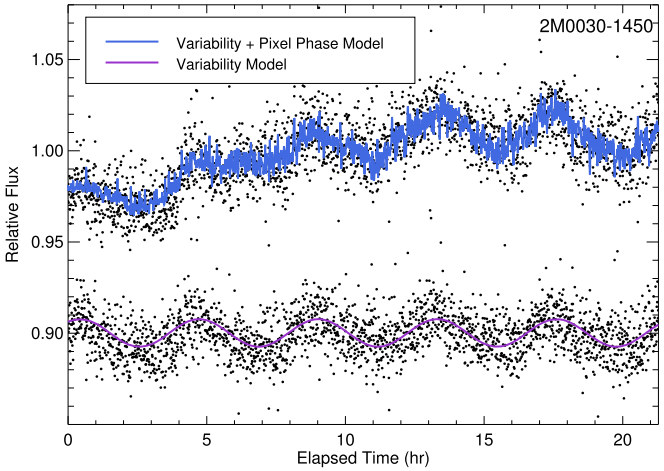

Figure 4. Raw light curve (top) and corrected light curve for 2MASS J0030−1450. The combined astrophysical variability and pixel phase model is shown in blue, and the astrophysical variability model is shown in purple.

Spitzer/IRAC photometry is known to exhibit a systematic effect due to intra-pixel sensitivity variations, also known as the pixel phase effect. Intra-pixel sensitivity variations, combined with telescope pointing fluctuations, result in raw photometry that is highly correlated with the x and y sub-pixel coordinates. We model the pixel phase effect using a cubic function of the x and y coordinates (Knutson et al. 2008; Heinze et al. 2013; Metchev et al. 2015; Vos et al. 2020):

$$f(x, y) = P_0 + P_1 x + P_2 y + P_3 xy + P_4 x^2 + P_5 y^2 + P_6 x^3 + P_7 y^3 + P_8 x^2 y + P_9 xy^2, \quad (1)$$

where $f(x, y)$ represents the measured flux, P_i are the fitted coefficients, and x and y are the sub-pixel coordinates. We correct the light curves of the target and reference stars using Equation (1), and find that the fitted coefficients P_i are similar for the target and reference stars. We find that the correction significantly decreases the correlation between the flux and pixel position for each observation. In Figure 4, we show an example target light curve before and after correction using the cubic function listed in Equation (1). This is the final step in producing corrected light curves.

3.1. Determining Variability Parameters Using MCMC

For objects showing variability (the process for identifying variability is presented in Section 4), we use the Markov Chain Monte Carlo (MCMC) `emcee` package (Foreman-Mackey et al. 2013) to constrain the variability parameters such as rotation period and variability amplitude. For the MCMC analysis, we use 1000 walkers with 8000 steps, and discard the initial 1000 steps as the burn-in sample. We check for convergence by visually inspecting the resulting chains for each parameter to ensure that they are consistent with Gaussian noise. Additionally, we check that there is no significant difference between the parameter constraints obtained from the first and second halves of each chain. Based on these two checks, we find that the model converges well for each variable light curve. We use a sinusoidal model for all of our targets, except for 2MASS J0030−1450 and 2MASS J0642+4101, whose light curves favor a two-term Fourier function. We show our measured variability parameters along with their 1σ

Table 3
Variability Parameters for Objects in the Survey

Name	SpT[a]	[3.6] Amp (%)	Period (hr)	Periodogram Power	$\Delta BIC_{flat-sin}$[b]	$\Delta BIC_{Mat3/2-Rot}$[c]
2MASS J0001+1535	L4β	0.69 ± 0.04	15.75 ± 0.37	85.4	114.3	41.3
2MASS J0030−1450	L7	1.52 ± 0.06	4.22 ± 0.02	182.3	572.2	2.4
J0031+5749	L9	0.35 ± 0.03	1.64 ± 0.01	40.8	73.6	23.7
2MASS J0153−6744	L2	0.48 ± 0.07	$17.63^{+1.13}_{-0.94}$	25.3	41.9	10.5
2MASS J0326−2102	L5β	0.34 ± 0.04	$32.84^{+4.60}_{-4.62}$	40.8	73.6	−4.4
2MASS J0342−6817	L4γ	0.73 ± 0.07	$14.73^{+0.51}_{-0.49}$	52.7	111.8	43.5
2MASS J0349+0635	L5γ	0.53 ± 0.09	$14.62^{+1.08}_{-1.00}$	16.8	23.4	30.1
2MASS J0355+1133	L5γ	0.26 ± 0.02	9.53 ± 0.19	85.2	85.2	20.7
2MASS J0447−1216	T2	<0.93	⋯	5.2	−9.1	⋯
2MASS J0459−2853	L7:	<0.47	⋯	4.7	−7.1	⋯
2MASS J0506+5236	T4.5	0.58 ± 0.10	$13.77^{+0.82}_{-0.77}$	17.1	21.7	23.1
2MASS J0642+4101	L9(red)	2.16 ± 0.16	10.11 ± 0.06	421.1	1317.8	49.9
2MASS J0718−6415	T5	2.14 ± 0.21	$1.080^{+0.004}_{-0.003}$	44.9 .2	47.5	
2MASS J0809+4434	L6p	0.77 ± 0.06	1.365 ± 0.004	79.1	185.3	61.2
2MASS J0951−8023	L5(pec)	<0.92	⋯	2.7	−12.4	⋯
2MASS J1551+0941	L4γ	<0.39	⋯	7.0	0.4	⋯
2MASS J1647+5632	L7	0.47 ± 0.06	$9.234^{+0.25}_{-0.23}$	32.0	52.7	2.8
2MASS J1741−4642	L6-L8γ	0.35 ± 0.03	$15.00^{+0.71}_{-0.57}$	45.5	96.1	32.9
2MASS J2002−0521	L5β	<0.28	⋯	12.1	−1.3	⋯
2MASS J2117−2940	T0	<0.38	⋯	4.6	−6.5	⋯
2MASS J2154−1055	L4β	<0.39	⋯	5.3	−8.2	⋯
2MASS J2206+3301	T1.5	1.20 ± 0.13	$15.91^{+0.62}_{-0.61}$	38.4	67.8	38.5
2MASS J2206−4217	L4β	<0.33	⋯	6.8	2.9	⋯
WISE J2216+1952	T3	<0.97	⋯	9.6	−15.6	⋯
2MASS J2322−6151	L2γ	<0.41	⋯	6.9	−5.4	⋯
2MASS J2343−3646	L3–L6γ	<0.37	⋯	3.6	−10.9	⋯

Notes.
[a] Spectral types and gravity classifications are from optical data unless only infrared was available.
[b] Positive $\Delta BIC_{flat-sin}$ values correspond to light curves preferred by the variable model over the flat model.
[c] Positive $\Delta BIC_{Mat3/2-Rot}$ values correspond to light curves preferred by the rotation model over the red noise model.

uncertainties in Table 3. Best-fit variability models are overplotted in pink in Figure 7.

We plot all of our variability detections on a color–magnitude diagram in Figure 3, where the symbol area is proportional to the amplitude of variability. This figure does not show any obvious trends between spectral type and amplitudes, and we observe a range of amplitudes throughout the L–T spectral sequence. We present a more in-depth discussion of variability amplitudes in Section 7.

4. Variability Analysis

Following the approach outlined in Vos et al. (2020), we use two independent methods to identify variable signals in each light curve—a periodogram significance test and the Bayesian Information Criterion (BIC). We briefly outline both methods below.

4.1. Variability Detection with Periodogram Analysis

We calculate the Lomb-Scargle periodograms of our target and reference starlight curves (Scargle 1982) to assess the significance of their brightness fluctuations. For each observation, we calculate the 95% and 99% significance thresholds by simulating non-variable light curves from our observed reference stars. The simulated, non-variable light curves are created by by randomly rearranging the indices of the reference starlight curves, which produces simulated light curves with Gaussian noise similar to our observed light curves. We consider a target to be variable only if the periodogram peak falls above the 99% significance threshold. For variable targets, we also perform a visual check to ensure that the periodicity of the object is not correlated with the periodicity of the x and y pixel coordinates. In Figure 5, we this comparison for the object 2MASS J0718−6415.

4.2. Variability Detection Using the Bayesian Information Criterion

We additionally use the BIC to identify significant variability in each observation (Schwarz 1978). The BIC is defined as

$$BIC = -2 \ln \mathcal{L}_{max} + k \ln N, \quad (2)$$

where $\mathcal{L}_{max}$ is the maximum likelihood achievable by the model, k is the number of parameters in the model, and N is the number of data points used in the fit (Schwarz 1978).

For each observation, we calculate $\Delta BIC = BIC_{flat} - BIC_{sin}$ to assess whether the variable sinusoidal or non-variable flat model is favored by the data. The BIC penalizes the sinusoidal model for having additional parameters compared with the flat model. $\Delta BIC > 0$ indicates that the sinusoidal model is favored, and $\Delta BIC < 0$ indicates that the non-variable, flat model is favored. A $|\Delta BIC|$ value between 0 and 6 indicates that one model is positively favored over the other, a value between 6 and 10 indicates that one model is strongly favored over the other, and values above 10

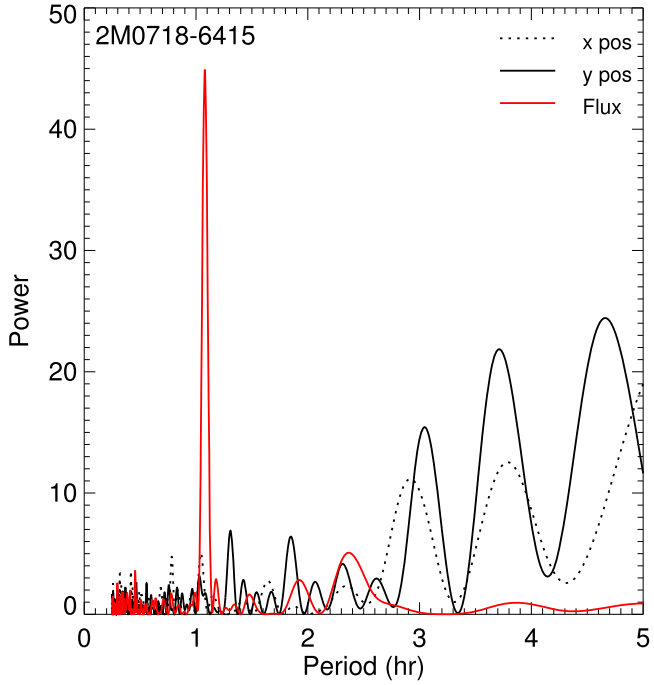

Figure 5. Periodogram of the light curve (red) as well as x and y pixel positions. For variable targets, we confirm that the periodicity is not correlated with the periodicity of the x and y pixel coordinates.

indicate that one model is very strongly favored over the other (Schwarz 1978). We conservatively consider light curves with $\Delta\mathrm{BIC} > 10$ to be a significant detection of variability for this survey.

We additionally use the BIC to determine whether any of our light curves favor a more complex variability model. For each light curve, we use the BIC to test both a sinusoidal model and a two-term Fourier model. Such models have been used to describe more complex brown dwarf light curves in the literature (Heinze et al. 2013; Yang et al. 2016; Vos et al. 2018), and may be driven by atmospheres with multiple atmospheric features and/or evolving cloud structures. We find that a two-term Fourier series is favored for two of our variable light curves: the L7 dwarf 2MASS J0030−1450 and the L9 dwarf 2MASS J0642+4101.

4.3. Comparison of ΔBIC and Periodogram Methods

In Figure 6, we compare the results of both variability identification methods. Objects placed in the upper right of the figure are considered variable by both methods, while objects in the lower left are classified as non-variable using both methods. We find that, in general, both methods agree on which light curves show significant variability as well as the relative significance of their variability detections. One object, 2MASS J2002−0521, is found to be variable using the periodogram method but not the ΔBIC test. We conservatively count it as non-variable for the remainder of the paper. We show our positive variability detections in Figure 7, and non-detections in Figure 8. In total, we detect variability in 15 objects, and do not detect variability in 11 objects.

4.4. Modeling Red Noise Contributions Using Gaussian Processes

While our two variability identification methods are in agreement, we must ensure that the detected variability is astrophysical in nature, and not due to correlated, or "red," noise. Red noise can mimic the signatures of astrophysical variability.

Littlefair et al. (2017) presents a framework to determine between astrophysical variability and red noise using Gaussian Processes (GPs). GPs have recently been used in the exoplanet and stellar subfields of astronomy to model both light-curve systematics and rotational modulations (e.g., Gibson et al. 2012; Aigrain et al. 2016; Littlefair et al. 2017; Angus et al. 2018).

For this work, we compare two GP models computed using the `celerite2` package (Foreman-Mackey et al. 2017; Foreman-Mackey 2018). The first exhibits variability driven by red noise, as modeled by the Matern-3/2 kernel:

$$k(\tau) = \sigma^2\left(1 + \frac{\sqrt{3}\,\tau}{\rho}\right)exp\left(-\frac{\sqrt{3}\,\tau}{\rho}\right), \tag{3}$$

where σ and ρ are the GP hyperparameters. The second model exhibits rotational variability as described by a kernel that is a mixture of two simple harmonic oscillator kernels given by:

$$\begin{aligned} Q_1 &= \frac{1}{2} + Q_0 + \delta Q \\ \omega_1 &= \frac{4\pi Q_1}{P\sqrt{4Q_1^2 - 1}} \\ S_1 &= \frac{\sigma^2}{(1+f)\omega_1 Q_1} \end{aligned} \tag{4}$$

for the primary term, and

$$\begin{aligned} Q_2 &= \frac{1}{2} + Q_0 \\ \omega_2 &= \frac{8\pi Q_1}{P\sqrt{4Q_1^2 - 1}} \\ S_2 &= \frac{f\sigma^2}{(1+f)\omega_2 Q_2} \end{aligned} \tag{5}$$

for the secondary term. Its hyperparameters are easier to interpret than those for the previous model. Here, σ represents the standard deviation of the process, P represents the primary period of variability, Q_0 represents the quality factor for the secondary oscillation, δQ is the difference between quality factors for the first and second modes, and f is the fractional amplitude of the secondary mode compared to the primary.

For each of our variable light curves, we use `emcee` (Foreman-Mackey et al. 2013) to fit the GP model and compare models using the ΔBIC framework described previously. For each model, we initialize 32 walkers and run for 5000 steps after discarding a 2000 burn-in sample. Most light curves are fit moderately well by both models, but the rotation model in particular has many parameters that are not constrained by the data, especially for the longer-period rotators. We present the $\Delta\mathrm{BIC}_{\mathrm{Mat3/2-Rot}}$ for objects identified as variable in Section 4.3 in Table 3. We find that all of the previously identified variables are preferred by the rotation model over the red noise model, apart from 2MASS J0326−2102, the target identified to

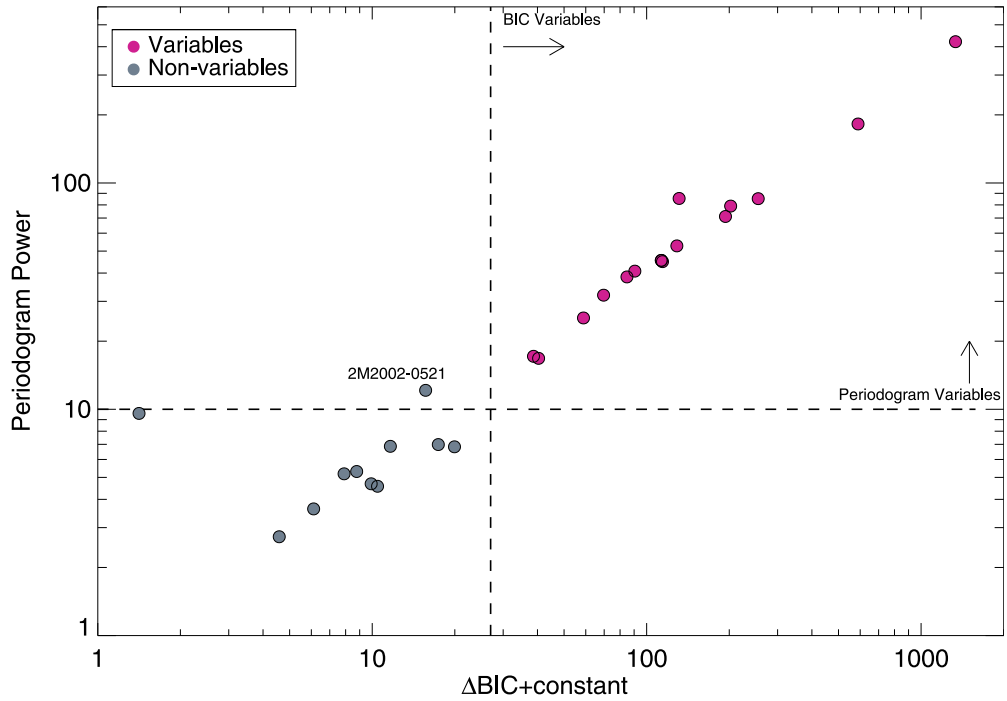

Figure 6. Periodogram power plotted against ΔBIC for all of our survey targets. Variable objects are shown in pink. Non-variable objects are shown in gray. A constant has been added to the ΔBIC values. The dashed lines show the significance thresholds for each test. Objects placed in the upper left of the figure are considered variable by both methods, while objects in the lower left are classified as non-variable using both methods. We find that both methods generally identify the same variables, except for the object 2MASS J2002−0521, which is significantly variable according the periodogram power method but not the Δ BIC test.

have a long period. The upward trend is fit equally well by both models, but the Matern-3/2 kernel is favored because it has fewer parameters. We conclude that this target requires longer-term monitoring to identify the cause of its upward flux trend, and therefore we leave it out of the statistical analysis.

4.5. Simultaneous Fit for Intra-pixel Sensitivity and Variability Parameters

The pixel-phase effect can, in principle, be covariant with astrophysical variability (e.g., Heinze et al. 2013). As described in Vos et al. (2020), we also perform a simultaneous fit of the intra-pixel phase effect (Equation (1)) and astrophysical variability. We again use the `emcee` package (Foreman-Mackey et al. 2013) to explore the parameter space. We find that fitting these effects simultaneously identifies the same variables and non-variables, as well as results in variability parameters that are broadly consistent with those presented in Table 3. However, for the simultaneous fit, we consistently find a higher correlation between the final light curve and the x, y pixel positions compared to the two-step fitting method; the Kendall τ correlation coefficient for the simultaneous fit can be up to an order of magnitude higher than the two-step method, and occasionally the correlation with pixel position increases compared to the raw flux. For this reason, we favor light curves corrected using the two-step method in this paper, as the corrected photometry is less likely to be affected by intra-pixel sensitivity.

4.6. Survey Sensitivity

We estimate the sensitivity of each observation to simulated sinusoidal variability following the methods outlined in Vos et al. (2019, 2020). We inject sinusoidal signals with a ranges of amplitudes and periods into light curves with Gaussian-distributed noise similar to that of each target. The simulated light curves have amplitudes of 0.05%–0.5%, rotation periods of 0.5–40 hr, and random phase shifts. We then analyze the simulated light curves using the periodogram analysis described in Section 4 and calculate the detection probability as the percentage of light curves with a given variability amplitude and period that produces a periodogram power above the significance threshold. Due to the range of magnitudes in our sample, the sensitivity of each observation can change significantly.

For non-variable targets, we determine an upper limit on the variability amplitude as the 90% contour boundary at 10 hr. Metchev et al. (2015) also set their upper limits assuming 10 hr periods, so our upper limits can be directly compared with their values. The left panel of Figure 9 shows the median sensitivity for the survey. Contours represent the rate of detection for signals of a given amplitude and period. The right panel of Figure 9 shows our calculated median sensitivity of the Metchev et al. (2015) survey for comparison, calculated in the same way. We note a slight improvement in the sensitivity of our survey compared to the Metchev et al. (2015). Both surveys have similar observation lengths (∼20 hr), and the median 3.6 μm magnitude for both samples is 13.1–13.2. The slightly higher sensitivity achieved by our survey is likely due to the fact that the Metchev et al. (2015) survey swapped between the [3.6 μm] and [4.5 μm] during each monitoring observation, or the differing data reduction and intra-pixel sensitivity correction methods. It is also possible that the amplitude of telescope motion for our observations was less than that of the Metchev et al. (2015) survey; the telescope drift during our ∼20 hr observations was consistently below 0.5 pixels for the observations presented in this survey, resulting in low-level intra-pixel effects. The sensitivity plot for each observation is

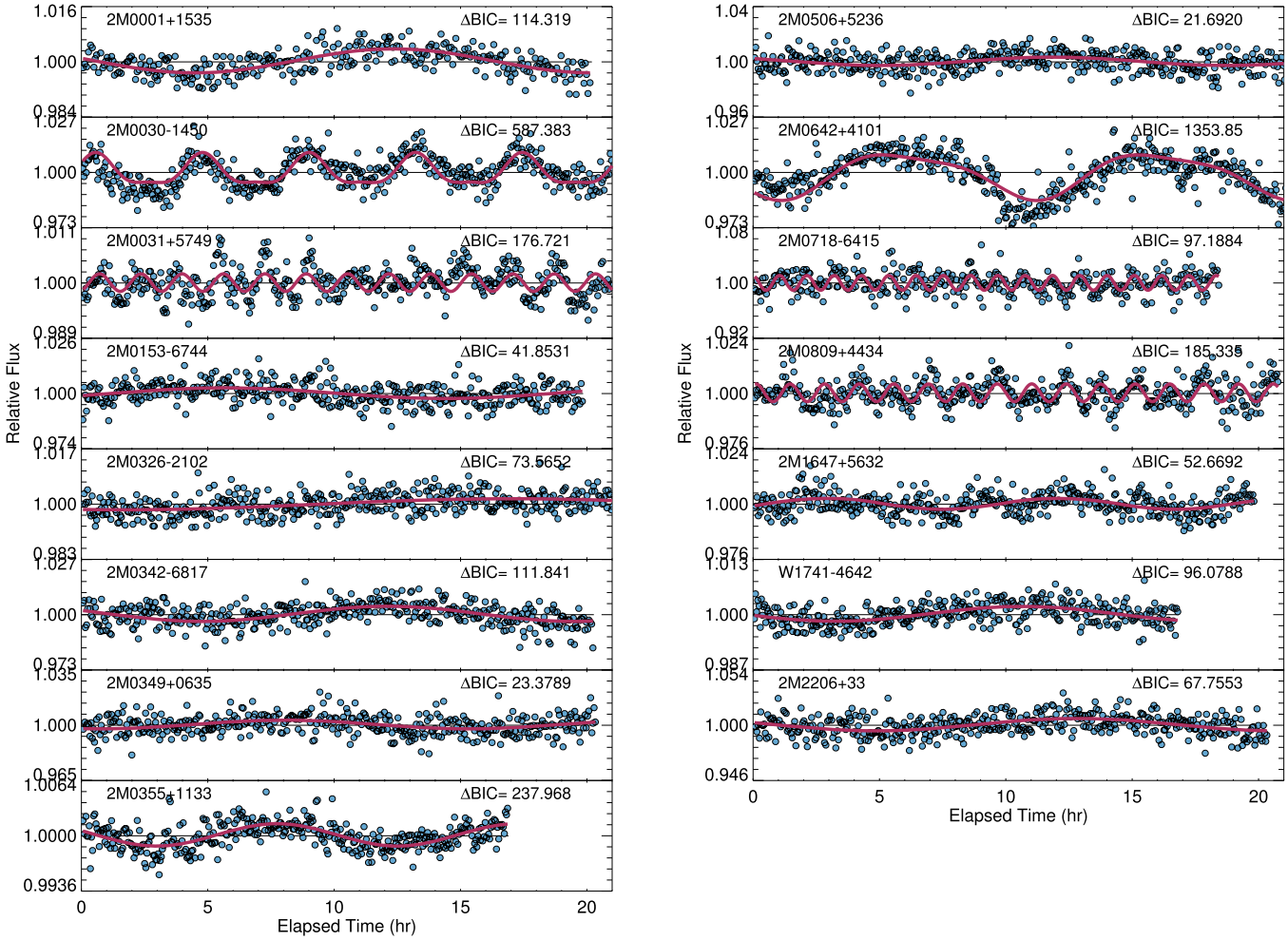

Figure 7. Positive variability detections from our survey. The blue points show 2.5 minutes cadence. ΔBIC values show that a variable model is favored in each case. A sinusoidal model is preferred for the majority of our variables, and a two-term Fourier series is favored for 2MASS J0030−1450 and 2MASS J0642+4101.

used in Section 6 to estimate the variability occurrence rates of young and field brown dwarfs.

5. Youth and Variability Properties of Individual Objects

In this section, we discuss the youth and variability properties of each object in the sample individually.

2MASS J0001+1535 was first identified as a candidate member of the AB Doradus moving group by Gagné et al. (2015c). They classify 2MASS J0001+1535 as an L4β spectral type, with an INT-G gravity score (Allers & Liu 2013). Faherty et al. (2016) classified 2MASS J0001+1535 as an ambiguous member because it lacked a parallax and radial velocity. With updated proper motion and parallax measurements from Gaia DR2 (Gaia Collaboration et al. 2018), we find that 2MASS J0001+1535 is a high-likelihood member of the AB Doradus moving group (Table 2). We note that the proper motions and a parallax presented in Best et al. (2020), which are within 2–3σ of the Gaia DR2 values, favor field over AB Doradus membership. Vos et al. (2019) monitored 2MASS J0001+1535 in their *J*-band survey, but did not detect variability above ∼2% during their 3.75 hr observation. In this work, we detect significant 3.6 μm variability with an amplitude of 0.69% ± 0.04% and a period of 15.75 ± 0.37 hr. Its long period likely prohibits detection in shorter observations —the sensitivity map for the light curve reported by Vos et al. (2019) shows that sinusoidal signals with amplitudes of >8%–10% would have been detected with a period ∼15 hr. Its long period is also consistent with other known variables from the AB Doradus moving group such as WISE J0047+68 (16.4 ± 0.2 hr; Vos et al. 2018).

2MASS J0030−1450 was given an optical classification of L7 by Kirkpatrick et al. (2000), an infrared spectral type of L4–L6β by Gagné et al. (2015c), and was assigned an FLD-G gravity class by Liu et al. (2016). Its kinematic measurements in Table 2 give it a high probability of membership in Argus according to BANYAN Σ. We classify it as a high-likelihood member of Argus. 2MASS J0030−1450 has been searched extensively for optical and infrared variability from ground-based telescopes in the literature (Enoch et al. 2003; Clarke et al. 2008; Radigan et al. 2014). Only Enoch et al. (2003) find a marginal detection of variability in the *i* band with a period of 1.5 hr. Clarke et al. (2008) and Radigan et al. (2014) report light curves with 1%–4% precision, and both works report no evidence for variability. We detect variability in its light curve, with an amplitude of 1.46% ± 0.06% and a rotation period of 4.29 ± 0.02 hr. The light curve appears stable over five rotations, but the non-detections reported in the literature to date suggest the possibility of an evolving light curve. 2MASS J0030−1450 is one of two variables whose light curves favor a two-term Fourier fit over a sinusoidal model.

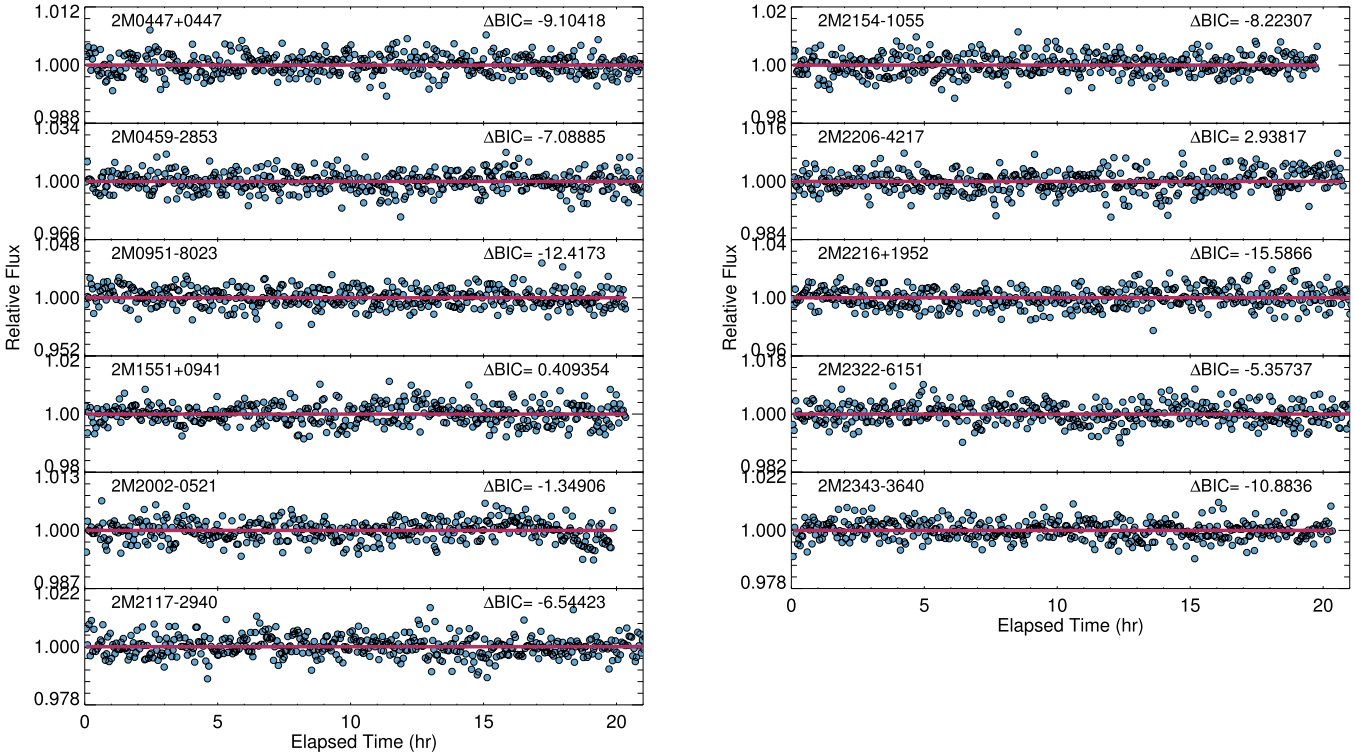

Figure 8. Non-detections of variability from our survey. The blue points show the light curve binned to 2.5 minutes cadence.

J0031+5749/PSO J282.7576+59.5858 was given an L9 spectral type by Best et al. (2013), who note that it is not matched well by any of their spectral templates. They suggest that the spectrum may be a blended spectrum of multiple objects; however, the spectral indices do not classify it as a binary. Best et al. (2020) also report a parallax of 71 ± 5 mas. Using the kinematic measurements in Table 2, BANYAN Σ reports that J0031+5749 is a high-likelihood member (98% probability) of the Carina-Near moving group. J0031+5749 has not been monitored for variability in the past. Our new Spitzer light curve reveals variability with an amplitude of $0.35\% \pm 0.03\%$ with a rotation period of 1.64 ± 0.01 hr. The light curve shows evidence of light-curve evolution during the 20 hr observations, with the amplitude ranging from ∼0.3%–1%. The periodogram shows two narrow peaks at ∼1.6 hr, which is suggestive of differential rotation (Apai et al. 2017). This target adds to the small but growing number of L/T transition brown dwarfs that show light-curve evolution on rotational timescales (e.g., Apai et al. 2017, 2021).

2MASS J0153−6744 was classified as an L3β with a VL-G gravity class by Gagné et al. (2015c), who also identified it as a likely member of the Tucana-Horologium moving group. Using the kinematics presented in Table 2, both BANYAN Σ and LACEwING identify it as a likely Tucana-Horologium member; however, parallax and radial velocity measurement are needed to confirm this object as a member. We classify 2MASS J0153−6744 as a candidate member of Tucana-Horologium. Our Spitzer light curve shows significant variability, with a $0.48\% \pm 0.07\%$ amplitude and a period of $17.63^{+1.13}_{-0.94}$ hr.

2MASS J0326−2102 has been identified as a highly probable member of AB Doradus by Gagné et al. (2014b), who also assign an L5 β/γ spectral type and note that the spectrum is very red for its spectral type. Cruz et al. (2007) suggest that 2MASS J0326−2102 is likely younger than 500 Myr, based on the strength of its Li absorption. Our updated kinematic analysis, which uses new proper motions from (Marocco et al. 2021), agrees with these findings. We classify 2MASS J0326−2102 as a high-likelihood member of AB Doradus, but a radial velocity is needed to confirm membership. Our Spitzer monitoring shows a slowly increasing brightness during the observations. The variability is highly significant, with a periodogram power of ∼40 and a ΔBIC of ∼74. Our MCMC variability fitting finds a period of 33 ± 5 hr; however, this is extremely uncertain because we did not cover a full period. The GP analysis presented in Section 4.4 finds that the signal may be explained by correlated red noise in the data. Whether the variability is rotationally modulated, related to a longer-term astrophysical process, or caused by systematics is an interesting question, which additional long-term monitoring will answer.

2MASS J0342−6817 is an L4γ with strong membership probability in the Tucana-Horologium association (Gagné et al. 2015c) and Faherty et al. (2016) classify it as a high-likelihood member. Using proper motions from Gagné et al. (2015b), we recover similar results, finding that BANYAN Σ favors membership in Tucana-Horologium. We classify 2MASS J0342−6817 as a high-likelihood member of Tucana-Horologium. The light curve of 2MASS J0342−6817 displays significant variability over the observation. With an estimated period of 14.7 ± 0.5 hr, we cover just over one rotation period during our Spitzer observation.

2MASS J0349+0635 is one of three likely young brown dwarfs presented in this work for the first time. As discussed in Section 2.1, 2MASS J0349+0635 is an L5γ, with prominent alkali absorption lines that are suggestive of low gravity. We use BANYAN Σ to assess membership using measured kinematic information. Based on sky positions and proper

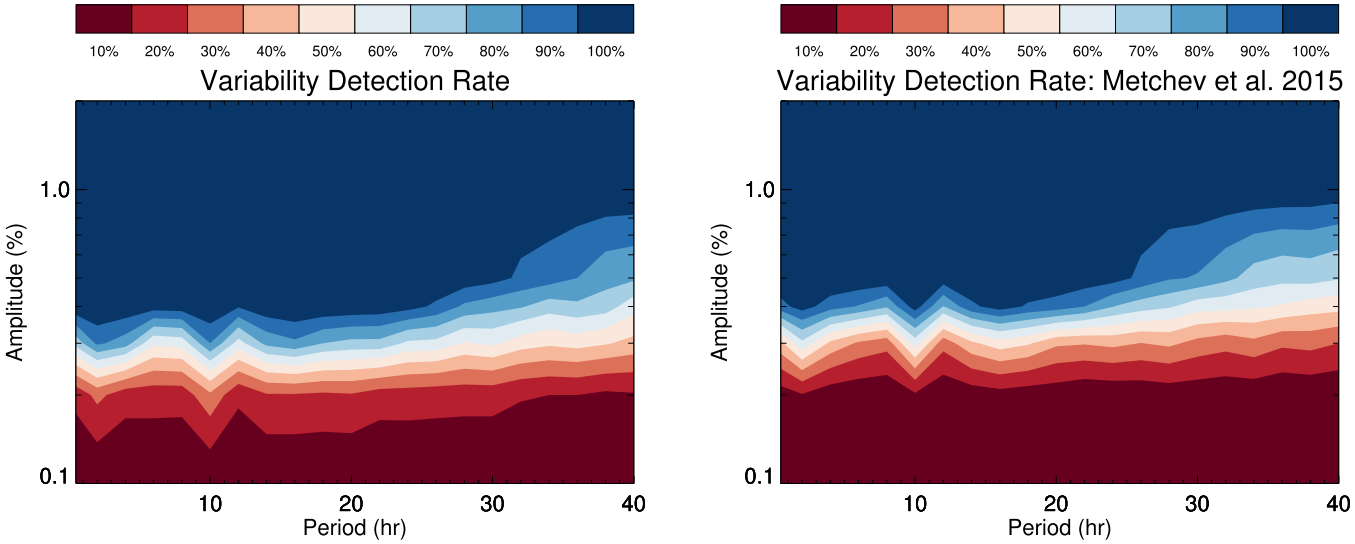

Figure 9. Median survey sensitivity as a function of variability amplitude and rotation rate for this survey (left) and the Metchev et al. (2015) survey. Contours show the percentage of recovered signals for each amplitude and period. The detection rates achieved by both variability surveys are very similar, and thus can be compared robustly. For non-variable objects, we assign upper limits on the variability amplitude as the 90% contour at 10 hr.

motions from (Marocco et al. 2021) (shown in Table 2), we find a combined probability of 75% that 2MASS J0349+0635 is a member of either AB Doradus or β Pictoris. Including the radial velocity measured from a FIRE/Echelle spectrum (J. Gagné et al. 2021, in preparation) reduces the probabilities of AB Doradus and β Pictoris membership to 25% and 19%, respectively. While the kinematic analysis does not conclusively identify moving group membership, the low-gravity signatures in its spectrum lend support to its likely youth. We consider 2MASS J0349+0635 as an ambiguous member for the remaining analysis. We detect significant variability in our Spitzer light curve, with an amplitude of $0.53\% \pm 0.09\%$ and a period of $14.62^{+1.1}_{-1.0}$ hr.

2MASS J0355+1133 is one of the prototypical isolated exoplanet analogs. It was identified as a high-likelihood member of the AB Doradus moving group by Faherty et al. (2013), and confirmed by follow-up measurements and analysis by Liu et al. (2016) and Faherty et al. (2016). Cruz et al. (2009) assign an L5γ spectral type. Faherty et al. (2013) noted its extremely red near-infrared colors and underluminosity compared to field brown dwarfs. These peculiarities were first noted by Metchev & Hillenbrand (2006) for the young companion HD203030 B (Miles-Páez et al. 2017), and are shared by directly imaged exoplanets such as 2M1207 b and HR8799 bcd. Our kinematic analysis, which makes use of Gaia proper motions and parallax, confirms that it is a member of AB Doradus using BANYAN Σ. We thus confirm 2MASS J0355+1133 as a bona fide member of AB Doradus. We measure significant variability in its 3.6 μm light curve. We measure a variability amplitude of $0.26\% \pm 0.02\%$ and a period of 9.53 ± 0.19 hr. 2MASS J0355+1133 joins W0047+68 and 2M2244+20 (Vos et al. 2018) as variable bona fide members of the AB Doradus moving group. We specifically focus on the variability properties of AB Doradus members in Section 9.

2MASS J0447−1216/PSO J071.8769–12.2713 was discovered by Best et al. (2015) as a T2 candidate of the β Pictoris moving group. Using BANYAN Σ, Best et al. (2020) measure new proper motions and parallax for this target, which determine that it is likely a field object. Proper motions from CatWISE2020 (Marocco et al. 2021) also agree that 2MASS J0447−1216 is likely a field object. We conclude that 2MASS J0447−1216 is likely a field object, and therefore we leave it out of the statistical analysis of variability in young objects in Section 6. In Figure 3, we plot our sample on a color–magnitude diagram and find that 2MASS J0447−1216 is overluminous compared to the field population; we speculate that this may be due to an unresolved binary companion, as suggested by Best et al. (2020). Vos et al. (2019) monitored this object for variability in ground-based *J*-band observations, detecting significant (4.5%) variability during a three-hour observation. Our Spitzer light curve does not display significant variability, and we place an upper limit of 0.9%. The variability detection in Vos et al. (2019) followed by a non-detection in this work suggests that 2MASS J0447−1216 may be a variable object whose light curve evolves over time. Such behavior has been observed in a number of variable L/T transition brown dwarfs (e.g., Apai et al. 2017). Another possibility is that 2MASS J0447−1216 exhibits variability that is only apparent in near-IR wavelengths, since different wavelengths probe different atmospheric layers.

2MASS J0459−2853 was discovered and classified as an L7 object with very red colors by Schneider et al. (2017). They note spectral features that are consistent with low surface gravity, but its kinematics did not match well with a young moving group. Our updated kinematics, which include proper motions from CatWISE2020 (Marocco et al. 2021) and a radial velocity from J. Gagné et al. (2021, in preparation), indicates that 2MASS J0459−2853 is a high-likelihood member of Argus. Its red near-IR colors, spectral signatures of youth, and spectral type are remarkably similar to other young, high-amplitude variables discovered to date, such as PSO J318.5−22 (Biller et al. 2015, 2018), VHS 1256 B (Bowler et al. 2020; Zhou et al. 2020), and WISE 0047+68 (Lew et al. 2016; Vos et al. 2018). We do not detect variability in the Spitzer light curve of 2MASS J0459−2853, and we place an upper limit of $<0.47\%$ on the peak-to-peak variability amplitude.

2MASS J0506+5236/PSO J076.7092+52.6087 was discovered and classified as a T4.5 spectral type by Best et al. (2015). Based on their measured proper motions, they determined that 2MASS J0506+5236 was a likely member of Argus. We check

for moving group membership using new proper motions and parallax from Best et al. (2020), which favor field membership with a 69% probability. Since this object has a T4.5 spectral type, we cannot examine the spectrum to look for signatures of youth, because such signatures are not yet known. We classify this object as a field object and do not include it in the following analysis sections. We detect variability in 2MASS J0506+5236 during our Spitzer observation, and we measure an amplitude of $0.6\% \pm 0.1\%$ and a rotation period of 13.8 ± 0.8 hr. Although its current kinematics favor field membership, its long rotation period is indicative of youth.

2MASS J0642+4101 was discovered by Mace et al. (2013) as an "extremely red" object at the L/T transition. Best et al. (2015) later assigned a L9 spectral type based on its *J*-band profile and the depth of its 2.4 μm water absorption feature. Its extremely red colors strongly suggest the presence of large amounts of dusty photospheric condensates (Best et al. 2015). Best et al. (2015) and Gagné et al. (2014b) both reported that 2MASS J0642+4101 is a likely AB Doradus member based on its proper motions and positions. Our analysis, which uses proper motions and a new parallax from Kirkpatrick et al. (2021), reports an 86% probability of AB Doradus membership. We thus consider it a candidate member of AB Doradus. With a measured variability amplitude of $2.16\% \pm 0.16\%$, 2MASS J0642+4101 shows the highest [3.6 μm] amplitude of any L dwarf measured to date, and is comparable to large amplitude [4.5 μm] variables such as PSO J318.5−22 (Biller et al. 2018). With a ∼10 hr period, we observe two full rotations during our Spitzer monitoring. During those two rotations, we see significant evolution in the light curve, including the emergence of a ∼1% dip with a 1 hr duration in the light curve at 15 hr. This dip may be due to the emergence of a Great Red Spot analog (Apai et al. 2017), or even a transiting satellite (Tamburo & Muirhead 2019; Limbach et al. 2021). Long-term follow-up observations could differentiate the cause of such dips in the light curve of 2MASS J0642+4101.

2MASS J0718−6415 Using the positions, proper motions, and radial velocity shown in Table 2, BANYAN Σ reports a membership probability of 85% for the β Pictoris moving group. Assuming it is a member of the β Pic moving group, we estimate a mass of $2.6 \pm 0.3\,M_{\rm Jup}$ using the SED analysis described in Section 8.1. Coincidentally, with a period of ∼1.08 hr, 2MASS J0718−6415 joins a T7 field brown dwarf, 2MASS J03480772−6022270 (hereafter 2MASS J0348−60), as the fastest rotating brown dwarfs detected to date (Tannock et al. 2021). 2MASS J0348−60 is estimated to be spinning at ∼45% of its break-up velocity. However, 2MASS J0718−6415 is likely young, and we have classified it as a candidate β Pictoris member. Using our estimated mass and radius from Table 4, we find that the break-up velocity for 2MASS J0718−6415 is ∼2.22 hr. Thus, if 2MASS J0718−6415 is indeed a β Pictoris member, it would be spinning faster than its theoretical break-up velocity. It is further possible that the observed variability pattern is produced by more than one dominant spatial feature, as for example seen with the regular positioning of near-equatorial hot spots on Jupiter (de Pater et al. 2016). Follow-up high-resolution spectroscopy will allow us to determine whether this object truly rotates so rapidly. Securing a parallax for 2MASS J0718−6415 and confirming its membership will reveal whether it is a very low-mass object that is potentially in the process of breaking up, or whether it is an older object rotating at a more moderate pace like 2MASS J0348−60.

2MASS J0809+4434 was identified by Gagné et al. (2015c) as an L6 pec (red) brown dwarf, and a candidate member of the Argus moving group. 2MASS J0809+4434 is classified with an INT-G gravity index following the Allers & Liu (2013) scheme. Best et al. (2020) provide a new parallax measurement of 42.4 ± 3.6 mas, which differs substantially from the predicted parallax of ∼65 mas assuming membership in Argus (Gagné et al. 2015c). Using this new parallax, BANYAN Σ reports 2MASS J0809+4434 as a field object. Due to its low-gravity spectral signatures, we consider 2MASS J0809+4434 to be a young field object. The Spitzer light curve of 2MASS J0809+4434 shows significant variability, with an amplitude of $0.77\% \pm 0.06\%$ and a period of 1.365 ± 0.004 hr.

2MASS J0951−8023 is one of the new brown dwarfs presented in this paper. As discussed in Section 2.1, we assign 2MASS J0951−8023 an L5(pec) spectral type. Using proper motions from CatWISE2020 (Marocco et al. 2021), and a radial velocity from J. Gagné et al. (2021, in preparation), our kinematics analysis classifies it as a candidate member of Argus, with an 87% BANYAN Σ probability. A parallax measurement is still necessary to confirm membership. We do not detect variability in the Spitzer light curve of 2MASS J0951−8023. We place an upper limit of 0.9% on its amplitude.

2MASS J1551+0941 shows clear signatures of youth in its spectrum. It has been classified as L4γ by Faherty et al. (2013) and L4 VL-G by Allers & Liu (2013). However, despite its clear spectral signatures of youth, 2MASS J1551+0941 is not an obvious member of any known moving group. Faherty et al. (2016) classified it as having ambiguous membership in young moving groups. Using an updated parallax from Gaia Collaboration et al. (2018) and an updated radial velocity from J. Gagné et al. (2021, in preparation), the BANYAN Σ tool reports that 2MASS J1551+0941 is likely a field object. Due to its strong youth indicators, we consider that 2MASS J1551+0941 is a young field object. The Spitzer light curve of 2MASS J1551+0941 does not show statistically significant variability during our 20 hr observation. We place an upper limit of 0.39% on the variability amplitude for periods of ∼10 hr.

2MASS J1647+5632 was discovered and classified as an L9 (pec) brown dwarf with a very red spectrum by Kirkpatrick et al. (2011). They report a parallax of 116 ± 29 mas. More recently, Best et al. (2020) report a parallax of 42.9 ± 2.1 mas, which is not in agreement with the original parallax measurement from Kirkpatrick et al. (2011). Kirkpatrick et al. (2011) identifies 2MASS J1647+5632 as a candidate member of β Pictoris or Argus, with a low probability of field membership. However, the updated parallax from Best et al. (2020) results in a 66% probability that 2MASS J1647+5632 is a field object, and 34% that it is a Carina-Near member. We classify 2MASS J1647+5632 as a young field object. We detect significant variability in our Spitzer light curve, and estimate a variability amplitude of $0.5\% \pm 0.1\%$ with a period of 9.2 ± 0.3 hr.

2MASS J1741−4642 was discovered and classified as L7 (pec) by Schneider et al. (2014). They also identified 2MASS J1741−4642 as a candidate member of either the AB Doradus or the β Pictoris moving group. Faherty et al. (2016) classify it as an L6–L8 γ based on its near-infrared spectrum. Recently, Kirkpatrick et al. (2021) provide a new parallax

Table 4
Fundamental Parameters for Sample from SED Analysis

Short Name	Parallax[a] (mas)	Membership	Age (Myr)	L_{bol} (dex)	T_{eff} (K)	Radius (R_{Jup})	Mass (M_{Jup})	log(g) (dex)
2MASS J0001+1535	31.6 ± 1.8	HLM ABDMG	110–130	−3.90 ± 0.05	1725 ± 5	1.22 ± 0.02	33 ± 4	4.73 ± 0.06
2MASS J0030−1450	41.1 ± 5.3	HLM ARG	30–50	−4.35 ± 0.11	1264 ± 78	1.36 ± 0.04	10 ± 2	4.12 ± 0.05
J0031+5749	71 ± 5.0	HLM CARN	150–250	−4.35 ± 0.06	1343 ± 58	1.2 ± 0.06	24 ± 7	4.60 ± 0.17
2MASS J0153−6744	(19.9 ± 1.2)	CAN THA	41–49	−3.80 ± 0.05	1664 ± 53	1.48 ± 0.03	17 ± 2	4.26 ± 0.03
2MASS J0326−2102	(42.7 ± 2.1)	HLM ABDMG	110–150	−4.25 ± 0.04	1359 ± 46	1.32 ± 0.06	18 ± 4	4.37 ± 0.11
2MASS J0342−6817	(19.4 ± 1.1)	HLM THA	41–49	−3.81 ± 0.05	1650 ± 51	1.48 ± 0.03	17 ± 2	4.26 ± 0.03
2MASS J0349+0635	…	AM	10–150	…	…	…	…	…
2MASS J0355+1133	109.6 ± 0.7	BF ABDMG	110–150	−4.12 ± 0.01	1527 ± 14	1.22 ± 0.02	28 ± 2	4.66 ± 0.05
2MASS J0447−1216	23 ± 3.9	FLD	500–1000	−4.28 ± 0.15	1521 ± 139	1.02 ± 0.07	51 ± 16	5.05 ± 0.22
2MASS J0459−2853	(32.2 ± 3.1)	HLM ARG	30–50	−4.54 ± 0.15	1152 ± 98	1.32 ± 0.03	8 ± 1	4.06 ± 0.06
2MASS J0506+5236	59.6 ± 5.4	FLD	500-1000	−4.87 ± 0.08	1065 ± 63	1.05 ± 0.08	26 ± 7	4.74 ± 0.20
2MASS J0642+4101	62.6 ± 3.1	CAN ABDMG	110–150	−4.64 ± 0.02	1124 ± 11	1.23 ± 0.0	12 ± 1	4.28 ± 0.01
2MASS J0718−6415	(107 ± 11)	CAN BPMG	16–28	−5.70 ± 0.09	596 ± 32	1.29 ± 0.02	3 ± 1	3.57 ± 0.07
2MASS J0809+4434	42.4 ± 3.6	YNG-FLD	10–150	−4.37 ± 0.07	1253 ± 74	1.35 ± 0.11	13 ± 8	4.12 ± 0.36
2MASS J0951−8023	(17.2 ± 1.4)	CAN ARG	30–50	−4.04 ± 0.07	1463 ± 65	1.45 ± 0.05	15 ± 2	4.22 ± 0.07
2MASS J1551+0941	22.1 ± 1.5	YNG-FLD	10–150	−3.86 ± 0.06	1653 ± 126	1.39 ± 0.19	24 ± 14	4.41 ± 0.40
2MASS J1647+5632	42.7 ± 2.1	YNG-FLD	150–250	−4.47 ± 0.04	1244 ± 47	1.22 ± 0.07	18 ± 6	4.45 ± 0.19
2MASS J1741−4642	50.5 ± 2.9	BF ABDMG	110–150	−4.17 ± 0.05	1471 ± 44	1.23 ± 0.02	26 ± 3	4.63 ± 0.07
2MASS J2002−0521	56.7 ± 1.5	YNG-FLD	10–150	−4.30 ± 0.02	1301 ± 56	1.36 ± 0.11	13 ± 8	4.14 ± 0.34
2MASS J2117−2940[b]	52.4 ± 6.8	AM/HLM BPMG	16–28	−4.44 ± 0.11	1192 ± 80	1.38 ± 0.05	7 ± 2	3.95 ± 0.12
	76.1 ± 3.5	AM/FLD	500–1000	−4.77 ± 0.04	1130 ± 50	1.05 ± 0.08	27 ± 7	4.75 ± 0.21
2MASS J2154−1055	32.6 ± 1.0	CAN CARN	150–250	−4.14 ± 0.03	1539 ± 31	1.17 ± 0.03	33 ± 4	4.76 ± 0.08
2MASS J2206+3301	(35.8 ± 2.4)	CAN ARG	30–50	−4.67 ± 0.06	1076 ± 37	1.3 ± 0.02	8 ± 1	4.03 ± 0.05
2MASS J2206−4217	33.8 ± 1.8	HLM ABDMG	110–150	−3.95 ± 0.05	1684 ± 46	1.22 ± 0.02	32 ± 3	4.72 ± 0.06
WISE J2216+1952	(44.2 ± 3.9)	CAN BPMG	16–28	−4.95 ± 0.08	909 ± 41	1.32 ± 0.02	5 ± 1	3.79 ± 0.12
2MASS J2322−6151	23.2 ± 1.0	BF THA	41–49	−3.71 ± 0.04	1740 ± 43	1.5 ± 0.03	18 ± 2	4.27 ± 0.04
2MASS J2343−3646	(24.7 ± 1.4)	CAN ABDMG	110–150	−3.87 ± 0.05	1755 ± 53	1.22 ± 0.02	34 ± 4	4.74 ± 0.06

Notes. The fundamental parameters listed in this table assume membership in the groups listed in the "Membership" column. Fundamental parameters for candidate and ambiguous members should be treated with caution because their membership is uncertain and may change with updated kinematics.
[a] Parallaxes in parentheses are kinematic distances that assume moving group membership indicated in the membership column.
[b] 2MASS J2117−2940 has two discrepant parallax values that result in either high-likelihood β Pictoris membership or field membership. We show fundamental parameters for both cases in this table for completeness.

measurement, and report a high probability that 2MASS J1741−4642 is a member of AB Doradus. Our updated analysis, which uses the parallax from Kirkpatrick et al. (2021) and a new radial velocity from J. Gagné et al. (2021, in preparation) confirms 2MASS J1741−4642 as a member of the AB Doradus moving group, with probability of 99% using BANYAN Σ. This agrees well with the signatures of youth in its spectrum (Schneider et al. 2014; Faherty et al. 2016). We detect significant variability in the Spitzer light curve of 2MASS J1741−4642, with an amplitude of 0.35% ± 0.03% and a period of $15.0^{+0.7}_{-0.6}$ hr. Vos et al. (2019) previously monitored 2MASS J1741−4642 in the *J* band and did not detect significant variability during a ∼2.5 hr observation. However, the sensitivity plot from this observation shows a very small probability (∼5%) of detecting variability with a period of 15 hr. Its rotation period matches well with the other late-L AB Doradus bona fide members with periods of 9–16 hr (W0047+68, 2M2244+20 (Vos et al. 2018), and 2MASS J0355+1133 (this work)), suggesting a common angular momentum history for these objects. We discuss 2MASS J1741−4642 in context with other AB Doradus members in Section 9.

2MASS J2002−0521 was classified as an L5-L7γ by Gagné et al. (2015c), but multiple studies have been unable to place it in a young moving group (Gagné et al. 2015c; Faherty et al. 2016; Vos et al. 2019). Our updated kinematics, which includes a new parallax from Gaia DR2 (Gaia Collaboration et al. 2018) similarly do not place it within a known moving group. However, its spectrum displays clear signature of youth, so we classify it as a young field object. Vos et al. (2019) detect *J*-band variability in this object using UKIRT/WFCAM, but the 4 hr observation did not yield periodicity. Its Spitzer light curve does not show significant variability, and we place an upper limit of 0.3% on 3.6 μm. Follow-up observations may reveal whether 2MASS J2002−0521 shows periods of variability followed by "quiescent" phases, such as those objects reported by Apai et al. (2017).

2MASS J2117−2940/PSO J319.3102-29.6682 was discovered and classified as a T0 dwarf by Best et al. (2015). More recently, Best et al. (2020) measured a parallax of 52.4 ± 6.8 mas for this object, and they report a BANYAN Σ probability of 99% that is a member of the β Pictoris moving group. However, Kirkpatrick et al. (2021) report a parallax of 76.1 ± 3.5 mas, which gives a 99% probability that 2MASS J2117−2940 is a field object. We do not include 2MASS J2117−2940 as a young object in the statistical analysis of variability Section 6, because its membership is unclear. However, in Section 8.1, we estimate fundamental parameters for this object for both cases, for completeness. We do not detect significant variability in the Spitzer light curve of 2MASS J2117−2940, and we place an upper limit of 0.38% on its amplitude.

2MASS J2154−1055 was identified as an L5 β/γ candidate member of the Argus moving group by Gagné et al. (2014a, 2015c). Vos et al. (2019) later identified it as a likely

member of the Carina-Near moving group. Our updated kinematic analysis finds that BANYAN Σ favors Carina-Near membership, with a membership probability of 80%. We thus classify 2MASS J2154−1055 as a candidate Carina-Near member. 2MASS J2154−1055 was monitored for *J*-band variability by Vos et al. (2019), who find no evidence for variability during a ∼4 hr observation. Similarly, our Spitzer light curve does not display any variability during our 20 hr observation, and we place an upper limit of 0.4% on the variability amplitude of this object.

2MASS J2206+3301/PSO J331.6058+33.0207 was discovered and identified as a T1.5 candidate Argus member by Best et al. (2015) based on its kinematics. Our analysis, which uses the proper motions from Best et al. (2015), finds that BANYAN Σ favors Argus (68%). We note that CatWISE2020 (Marocco et al. 2021) report discrepant proper motions for this target, resulting in a higher probability of field membership. For this work, we classify 2MASS J2206+3301 as a candidate Argus member. A future radial velocity and parallax measurement will help to clarify membership. We detect significant variability in 2MASS J2206+3301 with an amplitude of $1.2\% \pm 0.1\%$ and a period of 15.9 ± 0.6 hr. This is one of the longest rotation periods measured for any T dwarf, and adds further support that 2MASS J2206+3301 may be young.

2MASS J2206−4217 was discovered and classified as an L2 dwarf by Kirkpatrick et al. (2000). Kirkpatrick et al. (2008) detected lithium in its spectrum, and Gagné et al. (2014b) report it as a candidate AB Doradus member. Our updated kinematics analysis, which include new proper motions and a parallax from Gaia DR2 (Gaia Collaboration et al. 2018), confirms 2MASS J2206−4217 as a high-likelihood member of AB Doradus. A radial velocity is needed to confirm its membership. We do not detect variability in our Spitzer light curve of 2MASS J2206−4217, and place an upper limit of 0.33% on the variability amplitude.

WISE *J2216+1952/PSO J334.1+19* was discovered and identified as a T3 dwarf by Best et al. (2015), who identify it as a possible comoving companion to the M4 star LSPM J2216 +1952. They find that both components are candidate members of β Pictoris. Our independent kinematics analysis, which uses proper motions from CatWISE2020 (Marocco et al. 2021), finds a slightly higher BANYAN Σ β Pictoris membership probability (85%), and we classify it as a candidate β Pictoris member. We also repeat the BANYAN Σ analysis for the potential comoving primary LSPM J2216+1952 using new Gaia DR2 (Gaia Collaboration et al. 2018) proper motions and parallaxes; this analysis reports a 99% probability that it is a field star. Thus, we conclude that WISE J2216+1952 is a candidate β Pictoris member, but is likely not a companion to the star LSPM J2216+1952. We do not detect variability in our Spitzer light curve of WISE J2216+1952, and place an upper limit of 1% on the variability amplitude.

2MASS J2322−6151 is an L2γ (Gagné et al. 2014b) that was identified as a possible comoving companion to the M5 star 2MASS J23225240-6151114. Faherty et al. (2016) classify this object as a high-likelihood member of Tucana Horologium. Our updated kinematic analysis combines new proper motions and a parallax from Gaia DR2 (Gaia Collaboration et al. 2018) with a radial velocity measurement from Faherty et al. (2016) to confirm it as a member of the Tucana Horologium moving group. The primary, which lacks a radial velocity, shows a 99% membership in Tucana Horologium also. Thus, we confirm that 2MASS J2322−6151 is a member of the Tucana Horologium moving group and consider it highly likely that it is comoving with the M5 star 2MASS J23225240–6151114. This system will be the subject of an upcoming paper (J. K. Faherty et al. 2021, in preparation). We do not detect variability in our Spitzer monitoring of 2MASS J2322−6151, and we place a limit of 0.4% on the maximum variability amplitude for this object.

2MASS J2343−3646 was discovered and classified as an L3–L6γ dwarf, with a spectrum very similar to 2MASS J0355 +1133. Faherty et al. (2016) identify it as an ambiguous moving group member, which shows probability of membership in the AB Doradus and Tucana Horologium moving groups. We use proper motions from CatWISE2020 (Marocco et al. 2021) in our updated kinematic analysis. BANYAN Σ shows moderately high probability of membership in AB Doradus. We classify it as a candidate AB Doradus member. We do not detect significant variability in our Spitzer light curve of 2MASS J2343−3646, and we place an upper limit of 0.4% on its variability amplitude.

6. The Variability Occurrence Rate of Young Brown Dwarfs in the Mid-infrared

Our variability detections and detection limits can be used to estimate the fraction of young brown dwarfs that exhibit photometric variability (Vos et al. 2019). The occurrence rate analysis presented in this section is described by Lafreniere et al. (2007) and Bonavita et al. (2013), and is summarized below.

6.1. Statistical Formalism

We consider variability monitoring observations of N sources enumerated by $j = 1....N$. Here, f is the fraction of objects that exhibit variability with amplitude and rotation period in the interval $[a_{\min}, a_{\max}] \cap [r_{\min}, r_{\max}]$. For this work, we consider amplitude ranges of 0.05%–3% and rotation periods of 0.5–40 hr. Here, p_j is the probability that such variability would be detected from each observation. To calculate p_j, we use the variability sensitivity maps, $g(a, r)$, shown in Figure 9. We integrate over $g(a, r)$, the considered range in amplitude and period, to obtain the probability of detecting a variable signal with $a_{\min} < a < a_{\max}$ and $r_{\min} < r < r_{\max}$ for target j:

$$p_j = \int_{a_{\min}}^{a_{\max}} \int_{r_{\min}}^{r_{\max}} g(a, r)\, da\, dr. \tag{6}$$

Using this notation, the probability of detecting variability in target j is the fraction of objects displaying variability multiplied by the probability that such variability would be detected, or fp_j. The probability of not detecting variability is $(1 - fp_j)$. We denote d_j the detections made by the observations, such that $d_j = 1$ for a positive variability detection for target j and $d_j = 0$ for a non-detection. Then the probability of observing a detection or non-detection for a given f is:

$$L(d_j|f) = \prod_{j=1}^{N} (1 - fp_j)^{1-d_j} (fp_j)^{d_j}. \tag{7}$$

According to Bayes' theorem, the a priori probability density, or prior distribution $p(f)$, and the likelihood function L, can be used to calculate the posterior distribution $p(f|d_j)$, the

probability density updated in light of the data:

$$p(f|d_j) = \frac{L(d_j|f)p(f)}{\int_0^1 L(d_j|f)p(f)\mathrm{d}f}. \quad (8)$$

Since there are no independent variability occurrence rate estimates available, we use an noninformative Jeffreys prior. As outlined in the Appendix, the suitable Jeffreys prior is given as:

$$J(f) = \sqrt{\sum_j \frac{p_j}{f(1-fp_j)}}. \quad (9)$$

We calculate the posterior probability distribution, $p(f|d_j)$, which represents the fraction of variable objects, or variability occurrence rate of brown dwarfs. We calculate credible intervals for the variability occurrence rate, f, for a given level of credibility, α. We follow the method outlined by Kraft et al. (1991) to calculate the confidence intervals $[f_{\min}, f_{\max}]$, i.e., the upper and lower boundaries for the variability occurrence rate. We calculate the confidence interval by solving for $[f_{\min}, f_{\max}]$ in the equations:

$$\alpha = \int_{f_{\min}}^{f_{\max}} p(f|d_j)df \quad (10)$$

and

$$p(f_{\min}|d_j) = p(f_{\max}|d_j). \quad (11)$$

For the case of a one-sided distribution, the upper or lower bound of the credible interval is found by solving:

$$\alpha = \int_{f_{\min}}^{1} p(f|d_j)df \text{ or } \alpha = \int_0^{f_{\max}} p(f|d_j)df. \quad (12)$$

We determine the 68% and 95% confidence intervals in this paper.

6.2. The Variability Occurrence Rates of L and T Spectral Type Objects

We calculate the posterior distribution functions of the variability occurrence rates for the low-gravity and field population of brown dwarfs using the low-gravity sample presented here and the field objects from Metchev et al. (2015). The Metchev et al. (2015) sample included eight low-gravity brown dwarfs, which were added to the low-gravity survey sample presented in this paper and excluded from the field sample. We discard the magnetically active brown dwarf 2MASSW J0036159+182110 because it was a known variable prior to the Metchev et al. (2015) survey. We also discard known binaries. Furthermore, we discard three targets from the low-gravity sample presented in this paper: 2MASS J0447−1216, 2MASS J0506+5236 and 2MASS J2117−2940, because their youth and kinematic membership are uncertain, as discussed in Section 5. We calculate the posterior distribution functions of the variability occurrence rate for L dwarfs (SpT <L9), L/T transition objects (L9 ⩽ SpT ⩽ T3.5) and T dwarfs (SpT >T3.5). We show the variability occurrence rates of the young (pink) and field (blue) samples in Figure 10, and we discuss each spectral type bin below.

6.2.1. L-Dwarf Variability Occurrence Rates

For field L dwarfs, we find a variability occurrence rate of 83%–100% (68% confidence). We find a variability occurrence rate of 81%–100% for the low-gravity L dwarfs, which is consistent with that of the field gravity L dwarfs. Thus, we find no evidence for an enhancement in variability occurrence rate for the low-gravity L dwarfs. This is in contrast to Vos et al. (2019), who find a higher J-band occurrence rate for the low-gravity objects. This apparent discrepancy could be due to the different wavelength regimes and/or different sensitivities of each survey. Vos et al. (2019) surveyed 30 low-gravity objects using ground-based J-band observations. The J-band probes deeper pressure levels than the Spitzer [3.6 μm] band used in this survey (Buenzli et al. 2012). The J-band flux arises from pressures of ∼10 bar, while the Spitzer [3.6 μm] band probes pressures of ∼1 bar. Any difference in the observed variability properties between these wavelength regimes may suggest that they are sensitive to different variability mechanisms that take place at different altitudes. Simultaneous spectroscopic variability monitoring ranging from the near-infrared to the mid-infrared is necessary to test this possibility. However, another significant difference is the increased sensitivity achieved by Spitzer surveys (Metchev et al. 2015, this work) compared to ground-based searches (Radigan et al. 2014; Wilson et al. 2014; Eriksson et al. 2019; Vos et al. 2019). The Spitzer surveys on average probe variability amplitudes that are a factor of ∼10 smaller than the ground-based surveys mentioned above, and thus offer a more complete picture of low-level variability. Ground-based surveys thus may probe the variability occurrence rates of high-amplitude variables, while the Spitzer surveys may probe a more complete picture of variability at low to high amplitudes.

6.2.2. L/T Transition Variability Occurrence Rates

At the L/T transition (L9–T3.5), field dwarfs show a lower variability occurrence rate compared to field L-dwarf behavior, with a range of 22%–64% (68% confidence interval). Metchev et al. (2015) report similar findings, using virtually the same sample (Metchev et al. (2015) combined young and field brown dwarfs for their analysis, whereas we removed low-gravity objects from the field dwarf sample). As discussed by Metchev et al. (2015), this is in apparent contrast with the ground-based J-band survey reported by Radigan et al. (2014), who find an enhancement in variability occurrence rate at the L/T transition compared to earlier Ls and later Ts. The reasons for this difference may be the same reasons outlined above—the different wavelength regimes and sensitivities for Spitzer and ground-based near-infrared variability surveys. In contrast to the field dwarfs, young L/T transition objects maintain their high variability rate in the range 85%–100%. These results suggest that there may be an enhanced variability occurrence rate of low-gravity L/T transition objects compared to their field brown dwarf counterparts. Interestingly, this tentative enhancement may also explain the apparent disagreement between the L/T transition variability occurrence rates between Radigan et al. (2014) and Metchev et al. (2015) discussed above. Radigan et al. (2014) find high-amplitude variability in 4/16 of their L9–T3.5 sample, resulting in a high occurrence rate of high-amplitude variables. However, two of these detections, SIMP J0136+09 and 2MASS J2139+02, have since been identified as planetary-mass members of the

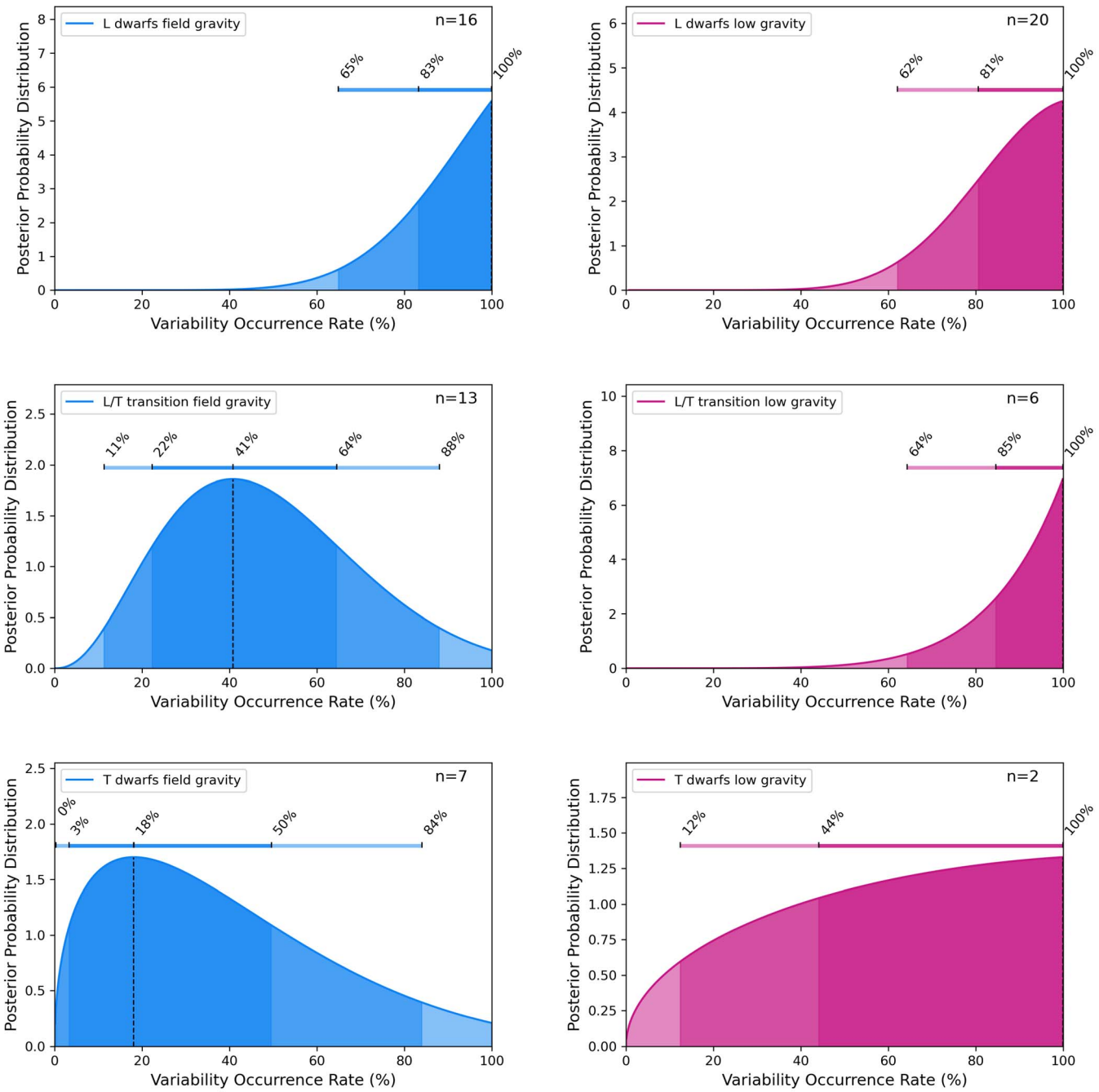

Figure 10. Posterior distribution functions of the variability occurrence rate of field brown dwarfs (blue) from Metchev et al. (2015) and young, low-gravity objects presented in this work. The shaded areas show the variability occurrence rate limits for the 95% and 68% confidence levels. Top panels show the occurrence rates for L dwarfs, the middle panel shows occurrence rates for the L/T transition, and the bottom panel shows the variability occurrence rates for T dwarfs.

Carina-Near moving group (Gagné et al. 2017; Zhang et al. 2021). Thus, a reanalysis of the Radigan et al. (2014) variability occurrence rates with updated youth information would be beneficial for evaluating whether field L/T transition objects have an enhanced variability rate.

6.2.3. T-Dwarf Variability Occurrence Rates

For field T dwarfs, the maximum likelihood value drops slightly (46% to 18%), but the confidence intervals (3%–50%) are generally consistent with the L/T transition objects. Metchev et al. (2015) explain the lower rate of variability for field T dwarfs as due to lower sensitivity to this sample, however since our calculations take into account the sensitivity of the sample, we do not believe that the low rate is due to lower sensitivity. For young T dwarfs, our sample is composed of only two T dwarfs—2MASS J0718−6415 (variable in this work) and Ross 458C, which is a known variable (Manjavacas et al. 2019), but was observed to be non-variable by Metchev et al. (2015), so it is classed as non-variable for our analysis. The resulting posterior distribution of the variability occurrence rate is wide, and we find that >44% of young objects with spectral types greater than T3.5 are likely to be variable at 68% confidence, >12% at 95% confidence. With the current sample, we cannot robustly compare between the variability occurrence

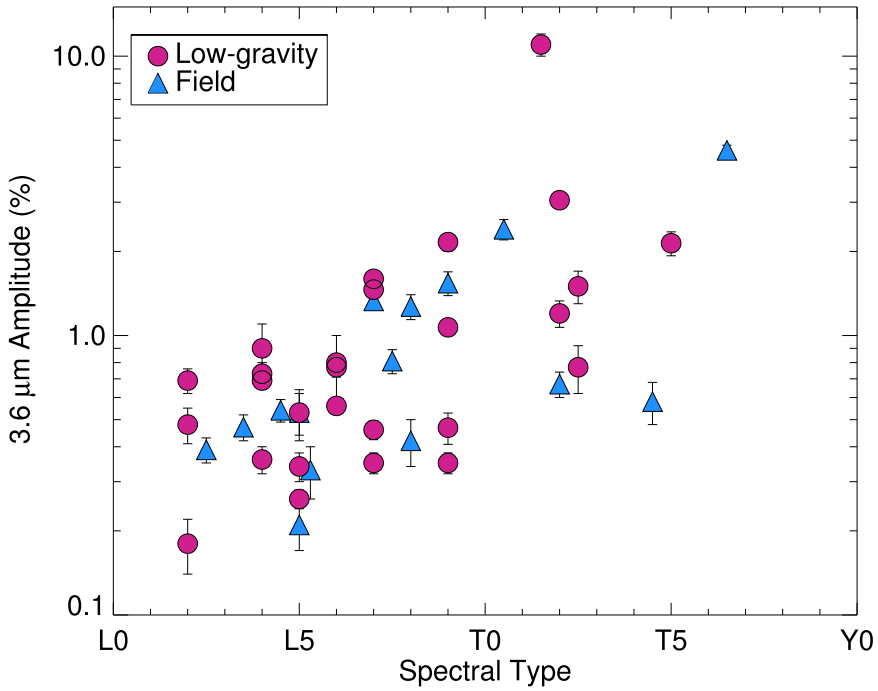

Figure 11. [3.6 μm] variability amplitudes of young objects (pink circles) and field objects (blue triangles) as a function of spectral type. Sources from this study and those compiled in Vos et al. (2020). As is the case for the field brown dwarfs (Metchev et al. 2015), the maximum variability amplitude of the young objects steadily increases with spectral type from early L to the L/T transition. It is also notable that the highest amplitude for each bin is measured for a young object for spectral types L0–L9. Thus, it seems that the *maximum* variability amplitudes of young brown dwarfs may be enhanced compared to field brown dwarfs.

rates of high- and low-gravity objects at spectral types $>T4$, but as more young T dwarfs are confirmed, this will be an interesting question.

7. The Variability Amplitudes of Young Brown Dwarfs at 3.6 micron

A number of studies have suggested that the variability amplitudes of low-gravity objects may be enhanced compared to the field brown dwarfs. (Biller et al. 2015; Metchev et al. 2015; Vos et al. 2020). Clouds in low-gravity atmospheres tend to form at lower pressures/higher altitudes (Marley et al. 2012), and thus higher-variability amplitudes might be expected due to a higher photometric contrast between regions of thick and thin clouds.

We combine the new variable objects detected in this survey with brown dwarfs previously monitored for [3.6 μm] variability with Spitzer (compiled in Vos et al. 2020) to investigate whether [3.6 μm] amplitudes are enhanced for low-gravity brown dwarfs. The T2.5 object 2MASS J2139+02 has been added to the young sample because it is a high-probability member of the Carina-Near moving group (Zhang et al. 2021). Figure 11 shows the [3.6 μm] variability amplitudes of the young (pink) and field (blue) L2–T5 brown dwarfs. As is the case for the field brown dwarfs (Metchev et al. 2015), the maximum variability amplitude of the young objects steadily increases with spectral type from early L to the L/T transition. The range of measured amplitudes in each spectral bin are generally consistent between the low-gravity and field dwarf populations. However, it is notable that the highest amplitude for each bin is measured for a young object for spectral types L0–L9. Thus, it seems that the *maximum* variability amplitudes of young brown dwarfs are enhanced compared to field brown dwarfs. These results suggest that variability amplitudes may be enhanced for low-gravity objects, but that secondary effects may affect the observed amplitudes. For example, the viewing inclination (e.g., Vos et al. 2017) likely reduces the observed variability amplitudes for objects viewed closer to pole-on, and may be responsible for the observed spread in amplitudes at each spectral type bin. Thus, the maximum variability amplitudes observed in low-gravity brown dwarfs would be higher than those of the field brown dwarfs, while both populations display variability down to the lower detection limit. Measuring the viewing angles of these low-gravity brown dwarfs with maximum amplitudes would allow us to test this possibility, and will be the focus of a future paper. Additionally, using three-dimensional atmospheric circulation models, Tan & Showman (2021) find that the rotation rate likely affects the size of atmospheric features in the atmosphere, and thus alters the variability amplitude driven by these features.

8. Rotation Rates of an Age-calibrated Sample

Identifying variable members of young moving groups is extremely valuable, as it provides an age-calibrated sample of young brown dwarfs with measured rotation rates, allowing us to trace angular momentum evolution (e.g., Scholz et al. 2018; Zhou et al. 2019; Vos et al. 2020). Of particular interest is whether there are rotational evolution trends related to mass, as is seen in our own solar system (e.g., Allers et al. 2016). We estimate masses for objects whose variability properties are presented in this paper (as described in the following section), and we gather estimated masses from the literature for the sample presented in Vos et al. (2020).

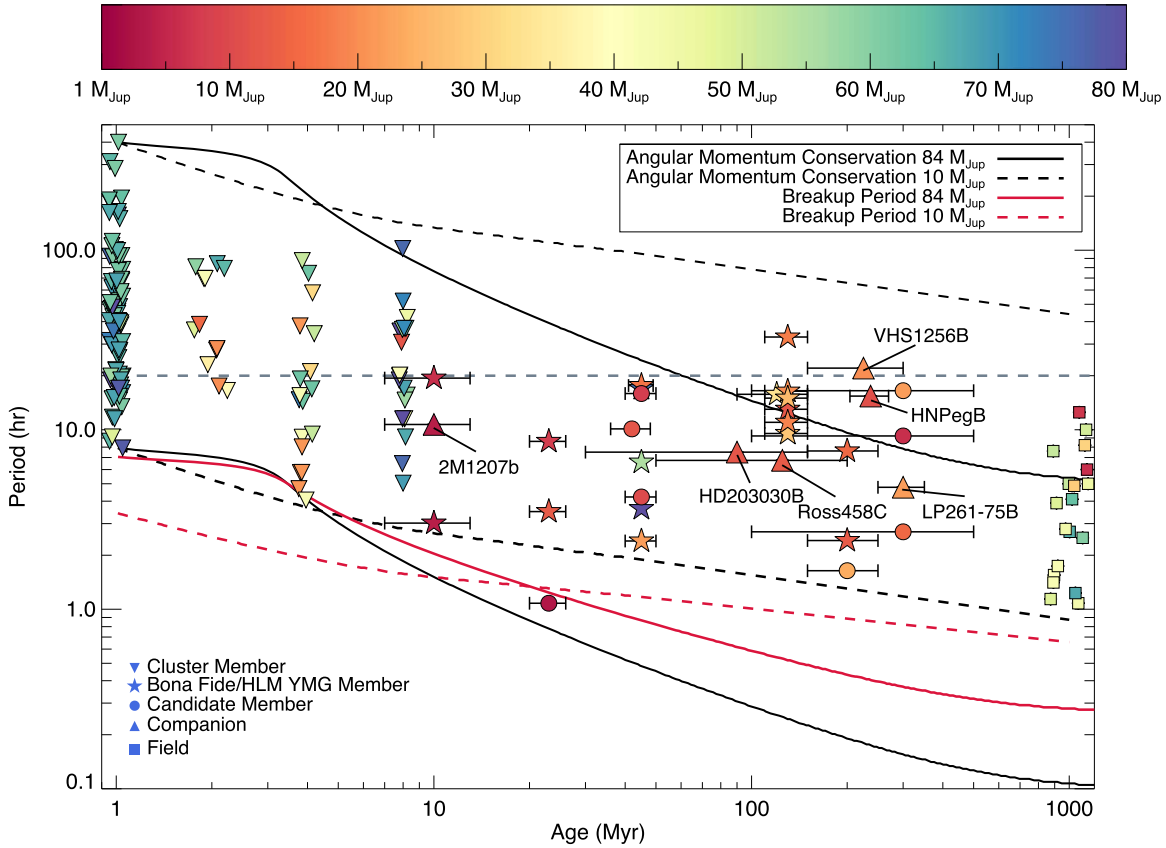

Figure 12. Brown dwarf rotation period as a function of age and color-coded by mass. Stars show bona fide and high-likelihood members of young moving groups, circles show candidate members of young moving groups, and squares show field brown dwarfs, which are plotted at 1 Gyr. Upside-down triangles are brown dwarf cluster members. Triangles show substellar companions with measured rotation rates. The 20 hr observation duration typically used by brown dwarf Spitzer variability studies is shown by the dashed line. While the higher-mass brown dwarfs (>30 $M_{\rm Jup}$) can be seen to spin up with age, this behavior is not observed in the low-mass sample (<30 $M_{\rm Jup}$), most likely because most low-mass objects lie in the intermediate age range. Companion brown dwarfs and planetary-mass objects at 10–500 Myr have rotation periods consistent with those of isolated objects with similar masses, indicating that they likely have similar formation pathways and subsequent angular momentum evolution histories.

8.1. Estimating Masses with Spectral Energy Distribution Analysis

We analyze the spectral-energy distributions (SEDs) of our young sample in order to investigate their fundamental parameters. We calculate the $L_{\rm bol}$, $T_{\rm eff}$, radii, masses, and log (g) following the method presented by Filippazzo et al. (2015). This method performs a numerical integration of the combined empirical visible and near-infrared photometry and spectra as well as WISE and/or Spitzer photometry, accessed through the BDNYC database (Filippazzo et al. 2016). We use parallaxes when available, but supplement with kinematic distances when a target is regarded as a high-likelihood member of a moving group. We present the fundamental parameters in Table 4. Our sample spans temperatures of ∼600–1750 K and model-dependent masses of 2.5–33 $M_{\rm Jup}$, overlapping with the masses and temperatures of the directly imaged exoplanets that have been discovered to date (e.g., Marois et al. 2008, 2010; Lagrange et al. 2010; Bohn et al. 2020, 2021).

8.2. Rotational Evolution as a Function of Time and Mass

In Figure 12, we show the current census of brown dwarf rotation rates as a function of age and color-coded by mass. The majority of objects were originally compiled in Vos et al. (2020). The 1–10 Myr sample was vetted and compiled by Moore et al. (2019) using *J*-band cutoffs to identify brown dwarfs. Scholz et al. (2018) calculate masses for the ∼2 Myr Taurus sample, and Scholz & Eislöffel (2004) provide masses for the ∼4 Myr σ Ori cluster sample. Although Rodríguez-Ledesma et al. (2009) estimate masses for the 1 Myr sample, those estimates are not provided in their paper. We estimate those masses by comparing their distance and reddening-corrected *I*-band magnitudes with the Baraffe et al. (2015) evolutionary models, as described by Rodríguez-Ledesma et al. (2009). Similarly, Moore et al. (2019) do not provide their estimated masses for the Upper Scorpius region. We estimate masses for this sample by comparing the targets' *J*-band magnitudes with the 10 Myr Baraffe et al. (2015) models, as described by Moore et al. (2019). For the Orion Nebula Cluster, the Orion Belt region, Upper Sco, and Taurus, we have added a random spread in the ages of each cluster member, for clarity. The rotation periods of brown dwarfs at age >10 Myr are compiled in Vos et al. (2020). We have added the measured rotation rates of young objects measured in this paper and those that have since been published by Tannock et al. (2021). Masses were either gathered from the literature (Faherty et al. 2016; Filippazzo et al. 2015) or estimated in this paper (Table 4). As described in Vos et al. (2020), we also plot angular momentum conservation tracks for objects with masses of 10 $M_{\rm Jup}$ and 84 $M_{\rm Jup}$ using the evolutionary models of Baraffe et al. (2015) as well as the breakup period for objects with these masses.

The majority of brown dwarf rotation rates >10 Myr have been measured with Spitzer, and many surveys including Metchev et al. (2015) and this work observe for ∼20 hr. We show this ∼20 hr cutoff as the gray dashed line in Figure 12. It is notable that we have detected a large number of variables in the 10–500 Myr age range with periods close to 20 hr, most notably a cluster of AB Doradus members with periods of 10–20 hr. This suggests that, by limiting our observation length, we are only sensitive to the fastest rotators and may be missing some variable brown dwarfs with rotation rates >20 hr. However, the high-variability occurrence rates achieved by large surveys suggest that the majority of rotation rates have been measured. Until we can probe longer rotation rates by observing on timescales of many days, it is important to keep in mind that we may not be measuring the full rotation rate distribution of brown dwarfs and/or isolated and companion planetary-mass objects.

We can also split the sample into two mass bins: the low-mass sample (<30 $M_{\rm Jup}$) and the high-mass sample (>30 $M_{\rm Jup}$). It is evident that the higher-mass brown dwarf sample spins faster with age, as expected from angular momentum conservation. However, the spin-up of the low-mass sample is not so evident. Based on the angular momentum conservation tracks shown in Figure 12, we expect that the high-gravity brown dwarfs should spin up more than their low-gravity counterparts. However, we do still expect to see some spin-up for the low-mass sample if we can probe a large enough age range. In particular, the long rotation periods of the two older planetary-mass Y dwarfs, WISE J085510.83-071442.5 and WISE J140518.8+553421.3 (Cushing et al. 2016; Esplin et al. 2016), are somewhat unexpected, as they are longer than the rotation periods of some planetary-mass objects at younger ages. However, the ∼10 hr rotation period of Jupiter suggests that the lowest-mass objects may maintain longer periods at older ages. A larger survey for variability in Y dwarfs (M. C. Cushing et al. 2021, in preparation) may help to provide more Y-dwarf rotation periods and reveal the rotational behavior of low-mass objects at old ages.

Finally, we have included companion objects with measured rotation rates (Zhou et al. 2016, 2018, 2020; Manjavacas et al. 2018, 2019; Miles-Páez et al. 2019; Bowler et al. 2020) in Figure 12, to investigate whether their angular momentum evolution may be different from the isolated objects focused on in this paper. Companion brown dwarfs and planetary-mass objects at ages 10–500 Myr have rotation periods consistent with those of isolated objects with similar mass, indicating that they likely have similar formation pathways and subsequent angular momentum evolution histories. A similar conclusion was reached by Bryan et al. (2018) based on rotational velocities of 11 low-mass objects. Based on our current data, it seems reasonable to use the observed distribution of planetary-mass brown dwarfs to estimate the expected rotation rates of directly imaged exoplanets when planning variability monitoring observations.

9. Variability Properties of AB Doradus Members

Within our sample, AB Doradus offers a unique opportunity to study the variability properties of a sample of coeval objects. Four objects in our survey are either bona fide or high-likelihood members of the AB Doradus moving group: 2MASS J0001+1535, 2MASS J0355+1133, 2MASS J1741−4642, and 2MASS J2206−4217. While the high-likelihood member 2MASS J0326−2102 was observed in this survey, its variability results are somewhat inconclusive, so we leave it out of the analysis. Four additional AB Doradus BF/HLM members have variability monitoring observations in the literature: WISE J004701.06+680352.1, 2MASS J2244316+204343, 2MASS J14252798−3650229, and SDSS 111010+011613 (Lew et al. 2016; Vos et al. 2018, 2020).

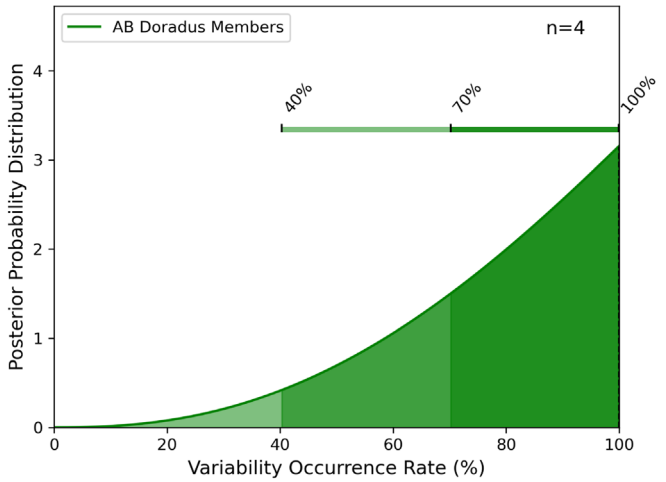

Figure 13. Variability occurrence rate of AB Doradus members in our sample. We determine that the variability occurrence rate for this sample is >76% at 68% confidence and >50% at 95% confidence.

9.1. Variability Occurrence Rate of AB Doradus

First, we use the methods outlined in Section 6 to determine the rate of variability for the four AB Doradus members in our sample. We did not include the other AB Doradus members presented in the literature, to avoid biasing our sample—some targets may have been observed with Spitzer after having been previously found to exhibit variability, while some non-detections may not have been published. We detect significant variability in 3/4 objects in our sample, with measured amplitudes from 0.3%–0.7%. We show the probability distribution of the variability occurrence rate for AB Doradus member in Figure 13. We determine that the variability occurrence rate for this sample is >70% at 68% confidence and >40% at 95% confidence. As we uncover more L- and T-type members of young moving groups, we can begin to compare occurrence rates across moving groups, and hence across ages.

9.2. Variability Amplitudes and Rotation in AB Doradus

In Figure 14, we show all ten HLM/BF substellar AB Doradus members that have been monitored in the Spitzer [3.6 μm] band, including this work and literature values from Vos et al. (2018, 2020), plotted on a spectral-type color diagram. We see a large range of [3.6 μm] amplitudes for this sample from 0.4%–3.1%. It seems that the observed variability amplitude increases as the temperature cools, at least from early-L to early-T spectral types. This behavior is also seen in Figure 11 for both the low-gravity and field-gravity populations, but it is notable that the amplitudes increase with decreasing temperature for a coeval population of young objects.

There is a very small range in the measured periods within AB Doradus; all of the variable objects have periods from 9–17 hr. This clustering of rotation periods is also evident in

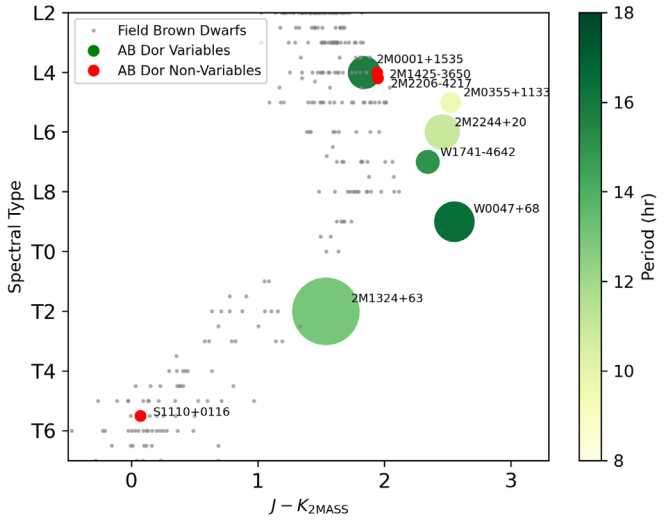

Figure 14. AB Doradus members monitored for variability in the Spitzer [3.6 μm] band. AB Doradus with detections of variability are shown in green, where the symbol size is proportional to the variability amplitude and the rotation rate is shown by color. Non-detections are shown in red. The field brown sample from Best et al. (2020) is shown in gray, for context.

Figure 12, where there is a pile-up of objects in this region. Since these objects are coeval, with similar masses, the similarity in their periods suggest that they share common angular momentum histories. Comparing these variability and rotation trends across other moving groups will help to reveal the diversity in the atmospheres of coeval objects. Moreover, combining Spitzer variability information for brown dwarfs with observations of high- to low-mass stars with the Transiting Exoplanet Survey Satellite (TESS) will allow us to trace variability properties and rotation from the highest- to lowest-mass products of star formation in a coeval sample.

10. Lessons for Variability Monitoring of Directly Imaged Exoplanets

One of the goals of this survey is to establish expectations for detecting variability in directly imaged exoplanets. There has been considerable success with variability searches in a handful of young wide-orbit companions with the WFC3 instrument on the Hubble Space Telescope (Zhou et al. 2016, 2019, 2020; Bowler et al. 2020; Lew et al. 2020) as well as some ground-based studies (e.g., Naud et al. 2017). Due to their close proximity to their host star and relative faintness, variability searches on directly imaged exoplanets such as HR8799 bcde and β Pic b present considerable challenges. To date, there have been two ground-based attempts to detect variability in HR8799 bc using the Very Large Telescope (VLT) (Apai et al. 2016; Biller et al. 2021); however, neither study reached the sensitivity to detect variability, placing near-infrared upper limits of 5%–10% on the variability amplitudes of the planets. Searching for variability in these exoplanets will likely require next-generation telescopes, such as the James Webb Space Telescope (JWST), and 30 m class telescopes, such as the European-Extremely Large Telescope (E-ELT), the Thirty Meter Telescope (TMT), and the Giant Magellan Telescope (GMT), which will provide unprecedented sensitivity for variability searches in directly imaged exoplanets. The survey presented here outlines baseline expectations for the behavior of exoplanets with similar temperatures, ages, and masses.

Our survey suggests that the directly imaged exoplanets are likely to have a high-variability occurrence rate across the full L and T spectral type regime. Our results also show that we can expect a large range of variability amplitudes for the directly imaged exoplanets with very large amplitudes for a subset of objects, potentially those with favorable viewing inclinations (e.g., Vos et al. 2017). Comparing the variability behavior of the directly imaged exoplanets with the low-mass sample presented in this paper will help to put each exoplanet in context with a larger sample of variables with similar temperatures, masses, and radii. Our survey also reveals the expected rotation periods for young, directly imaged exoplanets. With a median rotation period of $\sim$12 hr for young free-floating and companion objects, this work highlights the importance of long duration observations in order to measure a full period. For ground-based observations with the E-ELT, TMT, and/or GMT, multiple nights of observations may be necessary to capture the periodicity; however, the fastest rotators could be prioritized by measuring $v \sin(i)$ values prior to variability searches (Wang et al. 2021). Finally, ongoing variability surveys of Y dwarfs will be critical in revealing the potential for detecting variability in the coldest exoplanets (M. C. Cushing et al. 2021, in preparation).

11. Discussion and Conclusions

We have presented the most sensitive survey to date for variability in young, low-gravity, giant planet analogs. We surveyed 26 brown dwarfs with evidence of youth using the Spitzer Space Telescope at 3.6 μm, 23 of which we classify as young after a detailed study of their kinematic and spectroscopic evidence of youth. We report the discovery of three new brown dwarfs in this paper: 2MASS J0349+0635, 2MASS J0951−8023, and 2MASS J0718−6415, all of which show signatures of youth. Our variability analysis, which makes use of periodogram analysis and the Bayesian Information Criterion (BIC), identifies 15 variable and 11 non-variable objects in the full sample. We compare the variability properties of the low-gravity sample with those of their higher-mass field brown dwarf counterparts reported in the literature, specifically focusing on the variability occurrence rates, the variability amplitudes, and the rotation rates.

We determine the variability occurrence rates of young and field brown dwarfs in three spectral bins: L2−L8, L9−T3.5, and $\geqslant$T4. For L dwarfs, we find that both the young and field objects have variability occurrence rates of 80%–100%, i.e., virtually all L dwarfs are likely to be variable at the 0.05%–3% level. Our variability occurrence rate calculations find a tentative enhancement in the rate of variability in low-gravity objects with spectral types L9–T3.5 compared to the field dwarf populations with similar spectral types. The variability occurrence rate of low-gravity objects remains high from L to T dwarfs, while the occurrence rate appears to drop for field L/T transition and T dwarfs. The small sample size for young objects with spectral types $\geqslant$T4 prevents us from placing meaningful constraints on their variability occurrence rates. These results are encouraging for future high-contrast searches for variability in directly imaged exoplanets with JWST. While a number of ground-based searches have been carried out for the HR8799 planets (Apai et al. 2016; Biller et al. 2021) without detecting variability, JWST will provide unprecedented

sensitivity and precision. The results of these searches will be directly informed by the variability studies of isolated low-gravity brown dwarfs such as this one.

We find that the [3.6 μm] variability amplitudes increase steadily with spectral type from L to early T, as is observed for the field brown dwarfs (Metchev et al. 2015). This similar observed behavior supports our assumptions that the same variability mechanisms are at play in both samples. We also note that the maximum variability amplitudes observed for L dwarfs are higher for the low-gravity objects compared to the field objects. Atmospheric models predict that clouds are likely to form at higher altitudes in low-gravity atmospheres (Marley et al. 2012), and these higher clouds might result in a larger observed contrast between more cloudy and less cloudy regions. If this is the case, one might expect higher-variability amplitudes in the low-gravity sample. Indeed, there are a number of young brown dwarfs displaying extremely large amplitudes compared to their field brown dwarf counterparts such as 2MASS J2139+02 ($\sim$26% Radigan et al. 2012), VHS 1256 B ($\sim$25% Bowler et al. 2020; Zhou et al. 2020) and PSO J318.5−22 ($\sim$11% Biller et al. 2015). Our work shows that not every young brown dwarf exhibits such high amplitudes. We speculate that while the higher contrast from higher altitude clouds may result in higher intrinsic amplitudes, secondary effects such as viewing inclination (Vos et al. 2017) may be responsible for the range in amplitudes that we observe.

We combine our new rotation rates with those compiled by Vos et al. (2020), to investigate the angular momentum evolution of substellar objects from 1 Myr to >1 Gyr. First, we find that a large number of objects with ages 10–300 Myr have rotation periods close to 20 hr, which is the observation duration for many variability searches with Spitzer, including this work. This suggests that we may be missing the slowest rotators within this sample. Second, while the evolutionary spin-up of brown dwarfs with masses >30 $M_{\rm Jup}$ is evident, this process is not so clear for the lower-mass brown dwarfs (<30 $M_{\rm Jup}$). Measuring rotation rates of a larger number of low-mass brown dwarfs at ages <10 Myr and >1 Gyr (e.g., Y dwarfs) will help to reveal their spin-up properties over time and as a function of mass. We also compare the rotation rates of the small number of low-mass companion objects that have been monitored to date, finding that their rotation rates are consistent with those of the isolated low-mass brown dwarfs. These results suggest that we can base future variability monitoring observations of directly imaged exoplanets on the rotation rates measured to date for isolated low-mass brown dwarfs.

AB Doradus offers a unique opportunity to investigate the variability properties of a sample of coeval objects. Within AB Doradus, we find a variability occurrence rate of >70% and 68% confidence. We note that the amplitudes of AB Doradus members increase with decreasing temperature, as has been noted for field brown dwarfs (Metchev et al. 2015) and low-gravity sources (Vos et al. 2020, this work), but shown here for the first time in a coeval sample. We also note an apparent clustering of rotation periods for AB Doradus objects, with all of the measured periods in the range 9–17 hr. The similarity in their periods may suggest that these objects share common angular momentum histories. Comparing these variability trends across other moving groups will help to reveal how they change with age and mass.

Overall, the results from this survey are encouraging for variability searches in directly imaged exoplanets with future facilities such as JWST and 30 m telescopes, and the young brown dwarf sample presented here will serve as an excellent baseline for comparison. Variability monitoring observations with these facilities will enable unprecedented characterization of the weather phenomena and angular momentum properties and directly imaged exoplanets.

The authors would like to thank Azul Ruiz Diaz, Jai Glazer, and Sophia Ameneyro for their help and enthusiasm on this project through the NYC Science Research Mentoring Program at the American Museum of Natural History. We would like to thank the anonymous referee for thoughtful suggestions that significantly improved the paper. We would like to thank Dr. Seppo Laine and the Spitzer Science Center for their expertise and advice on Spitzer data products and analysis. This work is based on observations made with the Spitzer Space Telescope, which is operated by the Jet Propulsion Laboratory, California Institute of Technology under a contract with NASA. J. M. V. acknowledges support by NSF Award Number 1614527, Spitzer Cycle 14 JPL Research Support Agreement 1627378 and HST-GO-15924.001-A. J. V. and J.F. acknowledge support from the Heising-Simons Foundation. This work has made use of data from the European Space Agency (ESA) mission Gaia (https://www.cosmos.esa.int/gaia), processed by the Gaia Data Processing and Analysis Consortium (DPAC, https://www.cosmos.esa.int/web/gaia/dpac/consortium). Funding for the DPAC has been provided by national institutions, in particular the institutions participating in the Gaia Multilateral Agreement. This work has benefited from The UltracoolSheet, maintained by Will Best, Trent Dupuy, Michael Liu, Rob Siverd, and Zhoujian Zhang, and developed from compilations by Dupuy & Liu (2012), Dupuy & Kraus (2013), Liu et al. (2016), Best et al. (2018), and Best et al. (2020).

Facilities: Spitzer Space Telescope, Gaia DR2 (Gaia Collaboration et al. 2016, 2018), Magellan I FIRE (Simcoe et al. 2013).

BANYAN Σ (Gagné et al. 2018b), `SEDkit` (Filippazzo et al. 2015), `emcee` (Foreman-Mackey et al. 2013), `matplotlib` (Hunter 2007), `celerite2` (Foreman-Mackey et al. 2017).

Appendix
Jeffreys Prior Derivation

The Jeffreys prior is a noninformative prior that is invariant under parameter transformation. The Jeffreys prior is defined in terms of the Fisher information:

$$J(\theta) \propto \sqrt{I(\theta)}, \tag{A1}$$

where the Fisher information $I(\theta)$ is given by:

$$I(\theta) = -\mathbb{E}_\theta\left[\frac{d^2\ell}{d\theta^2}\right], \tag{A2}$$

where $\mathbb{E}$ represents the expectation value and $\ell$is the log likelihood. For the likelihood presented in Section 6, the Fisher

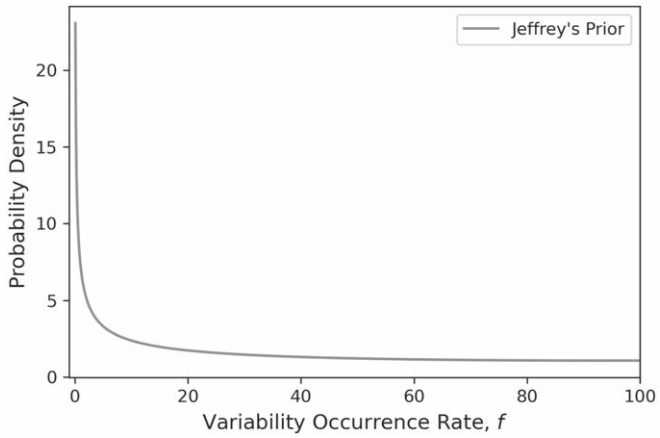

Figure 15. Jeffreys prior used for estimation of variability occurrence rate in Section 6.

information is given as:

$$I(f) = -\mathbb{E}_f\left[\sum_j \frac{d_j}{f^2 p_j} + \frac{p_j(1-d_j)}{(1-fp_j)^2}\right]. \quad \text{(A3)}$$

The expectation value of d_j is simply the fp_j, so the Fisher information can be expressed as:

$$I(f) = \sum_j \frac{p_j}{f(1-fp_j)}, \quad \text{(A4)}$$

and the Jeffreys prior is thus given as

$$J(f) = \sqrt{\sum_j \frac{p_j}{f(1-fp_j)}}. \quad \text{(A5)}$$

This represents a noninformative prior for estimation of the posterior distribution of the variability occurrence rate, f. We plot the prior in Figure 15.

ORCID iDs

Johanna M. Vos https://orcid.org/0000-0003-0489-1528
Jacqueline K. Faherty https://orcid.org/0000-0001-6251-0573
Jonathan Gagné https://orcid.org/0000-0002-2592-9612
Mark Marley https://orcid.org/0000-0002-5251-2943
Stanimir Metchev https://orcid.org/0000-0003-3050-8203
John Gizis https://orcid.org/0000-0002-8916-1972
Emily L. Rice https://orcid.org/0000-0002-3252-5886
Kelle Cruz https://orcid.org/0000-0002-1821-0650

References

Aigrain, S., Parviainen, H., & Pope, B. J. S. 2016, MNRAS, 459, 2408
Allers, K. N., Gallimore, J. F., Liu, M. C., & Dupuy, T. J. 2016, ApJ, 819, 133
Allers, K. N., & Liu, M. C. 2013, ApJ, 772, 79
Allers, K. N., Vos, J. M., Biller, B. A., & Williams, P. K. G. 2020, Sci, 368, 169
Angus, R., Morton, T., Aigrain, S., Foreman-Mackey, D., & Rajpaul, V. 2018, MNRAS, 474, 2094
Apai, D., Karalidi, T., Marley, M. S., et al. 2017, Sci, 357, 683
Apai, D., Kasper, M., Skemer, A., et al. 2016, ApJ, 820, 40
Apai, D., Nardiello, D., & Bedin, L. R. 2021, ApJ, 906, 64
Apai, D., Radigan, J., Buenzli, E., et al. 2013, ApJ, 768, 121
Artigau, É., Bouchard, S., Doyon, R., & Lafrenière, D. 2009, ApJ, 701, 1534
Baraffe, I., Homeier, D., Allard, F., & Chabrier, G. 2015, A&A, 577, 4
Barenfeld, S. A., Bubar, E. J., Mamajek, E. E., & Young, P. A. 2013, ApJ, 766, 6
Barman, T. S., Macintosh, B., Konopacky, Q. M., & Marois, C. 2011, ApJL, 735, L39
Bell, C. P. M., Mamajek, E. E., & Naylor, T. 2015, MNRAS, 454, 593
Best, W. M. J., Liu, M. C., Magnier, E. A., et al. 2013, ApJ, 777, 84
Best, W. M. J., Liu, M. C., Magnier, E. A., et al. 2015, ApJ, 814, 118
Best, W. M. J., Liu, M. C., Magnier, E. A., & Dupuy, T. J. 2020, AJ, 159, 257
Best, W. M. J., Magnier, E. A., Liu, M. C., et al. 2018, ApJS, 234, 1
Biller, B. A., Apai, D., Bonnefoy, M., et al. 2021, MNRAS, 503, 743
Biller, B. A., Crossfield, I. J. M., Mancini, L., et al. 2013, ApJL, 778, L10
Biller, B. A., Vos, J., Bonavita, M., et al. 2015, ApJL, 813, 1
Biller, B. A., Vos, J., Buenzli, E., et al. 2018, AJ, 155, 95
Blake, C. H., Charbonneau, D., & White, R. J. 2010, ApJ, 723, 684
Bohn, A. J., Ginski, C., Kenworthy, M. A., et al. 2021, A&A, 648, A73
Bohn, A. J., Kenworthy, M. A., Ginski, C., et al. 2020, ApJL, 898, L16
Bonavita, M., de Mooij, E. J. W., & Jayawardhana, R. 2013, PASP, 125, 849
Bowler, B. P., Zhou, Y., Morley, C. V., et al. 2020, ApJL, 893, L30
Bryan, M. L., Benneke, B., Knutson, H. A., Batygin, K., & Bowler, B. P. 2018, NatAs, 2, 138
Buenzli, E., Apai, D., Morley, C. V., et al. 2012, ApJL, 760, L31
Buenzli, E., Apai, D., Radigan, J., Reid, I. N., & Flateau, D. 2014, ApJ, 782, 77
Chauvin, G., Lagrange, A., Dumas, C., et al. 2004, A&A, 425, L29
Clarke, F. J., Hodgkin, S. T., Oppenheimer, B. R., Robertson, J., & Haubois, X. 2008, MNRAS, 386, 2009
Cruz, K. L., Kirkpatrick, J. D., & Burgasser, A. J. 2009, AJ, 137, 3345
Cruz, K. L., Núñez, A., Burgasser, A. J., et al. 2018, AJ, 155, 34
Cruz, K. L., Reid, I. N., Kirkpatrick, J. D., et al. 2007, AJ, 133, 439
Cushing, M. C., Hardegree-Ullman, K. K., Trucks, J. L., et al. 2016, ApJ, 823, 152
de Pater, I., Sault, R. J., Butler, B., DeBoer, D., & Wong, M. H. 2016, Sci, 352, 1198
Dupuy, T. J., & Kraus, A. L. 2013, Sci, 341, 1492
Dupuy, T. J., & Liu, M. C. 2012, ApJS, 201, 19
Enoch, M. L., Brown, M. E., & Burgasser, A. J. 2003, AJ, 126, 1006
Eriksson, S., Janson, M., & Calissendorff, P. 2019, A&A, 629, A145
Esplin, T. L., Luhman, K. L., Cushing, M. C., et al. 2016, ApJ, 832, 58
Faherty, J. K., Burgasser, A. J., Walter, F. M., et al. 2012, ApJ, 752, 56
Faherty, J. K., Rice, E. L., Cruz, K. L., Mamajek, E. E., & Núñez, A. 2013, AJ, 145, 2
Faherty, J. K., Riedel, A. R., Cruz, K. L., et al. 2016, ApJS, 225, 10
Fazio, G. G., Hora, J. L., Allen, L. E., et al. 2004, ApJS, 154, 10
Filippazzo, J. C., Giorla Godfrey, P., Cruz, K. L., et al. 2016, The BDNYC Database, 1.0, Zenodo, doi:10.5281/zenodo.45169
Filippazzo, J. C., Rice, E. L., Faherty, J., et al. 2015, ApJ, 810, 158
Foreman-Mackey, D. 2018, RNAAS, 2, 31
Foreman-Mackey, D., Agol, E., Ambikasaran, S., & Angus, R. 2017, AJ, 154, 220
Foreman-Mackey, D., Hogg, D. W., Lang, D., & Goodman, J. 2013, PASP, 125, 306
Gaia Collaboration, Brown, A. G. A., Vallenari, A., et al. 2018, A&A, 616, A1
Gaia Collaboration, Prusti, T., de Bruijne, J. H. J., et al. 2016, A&A, 595, A1
Gagné, J., Allers, K. N., Theissen, C. A., et al. 2018a, ApJL, 854, L27
Gagné, J., Burgasser, A. J., Faherty, J. K., et al. 2015a, ApJL, 808, L20
Gagné, J., Faherty, J. K., Burgasser, A. J., et al. 2017, ApJL, 841, L1
Gagné, J., Faherty, J. K., Cruz, K. L., et al. 2015c, ApJS, 219, 33
Gagné, J., Lafrenière, D., Doyon, R., et al. 2014a, ApJL, 792, L17
Gagné, J., Lafrenière, D., Doyon, R., Malo, L., & Artigau, É. 2014b, ApJ, 783, 121
Gagné, J., Lafrenière, D., Doyon, R., Malo, L., & Artigau, É. 2015b, ApJ, 798, 73
Gagné, J., Mamajek, E. E., Malo, L., et al. 2018b, ApJ, 856, 23
Gibson, N. P., Aigrain, S., Roberts, S., et al. 2012, MNRAS, 419, 2683
Hallinan, G., Littlefair, S. P., Cotter, G., et al. 2015, Natur, 523, 568
Heinze, A. N., Metchev, S., Apai, D., et al. 2013, ApJ, 767, 173
Hunter, J. D. 2007, CSE, 9, 90
Kao, M. M., Hallinan, G., Pineda, J. S., et al. 2016, ApJ, 818, 24
Kellogg, K., Metchev, S., Heinze, A., Gagné, J., & Kurtev, R. 2017, ApJ, 849, 72
Kirkpatrick, J. D., Cruz, K. L., Barman, T. S., et al. 2008, ApJ, 689, 1295
Kirkpatrick, J. D., Cushing, M. C., Gelino, C. R., et al. 2011, ApJS, 197, 19
Kirkpatrick, J. D., Gelino, C. R., Faherty, J. K., et al. 2021, ApJS, 253, 7
Kirkpatrick, J. D., Reid, I. N., Liebert, J., et al. 2000, AJ, 120, 447
Knutson, H. A., Charbonneau, D., Allen, L. E., Burrows, A., & Megeath, S. T. 2008, ApJ, 673, 526
Kraft, R. P., Burrows, D. N., & Nousek, J. A. 1991, ApJ, 374, 344

Lafreniere, D., Doyon, R., Marois, C., et al. 2007, ApJ, 670, 1367
Lagrange, A.-M., Bonnefoy, M., Chauvin, G., et al. 2010, Sci, 329, 57
Leggett, S. K., Cushing, M. C., Hardegree-Ullman, K. K., et al. 2016, ApJ, 830, 141
Lew, B. W. P., Apai, D., Zhou, Y., et al. 2016, ApJL, 829, L32
Lew, B. W. P., Apai, D., Zhou, Y., et al. 2020, AJ, 159, 125
Limbach, M. A., Vos, J. M., Winn, J. N., et al. 2021, ApJL, 918, L25
Littlefair, S. P., Burningham, B., & Helling, C. 2017, MNRAS, 466, 4250
Liu, M. C., Dupuy, T. J., & Allers, K. N. 2016, ApJ, 833, 96
Luhman, K. L., Patten, B. M., Marengo, M., et al. 2007, ApJ, 654, 570
Mace, G. N., Kirkpatrick, J. D., Cushing, M. C., et al. 2013, ApJ, 777, 36
Macintosh, B., Graham, J. R., Barman, T., et al. 2015, Sci, 350, 64
Manjavacas, E., Apai, D., Lew, B. W. P., et al. 2019, ApJL, 875, L15
Manjavacas, E., Apai, D., Zhou, Y., et al. 2018, AJ, 155, 11
Marley, M. S., Saumon, D., Cushing, M., et al. 2012, ApJ, 754, 135
Marocco, F., Eisenhardt, P. R. M., Fowler, J. W., et al. 2021, ApJS, 253, 8
Marois, C., Macintosh, B., Barman, T. S., et al. 2008, Sci, 322, 1348
Marois, C., Zuckerman, B., Konopacky, Q. M., Macintosh, B., & Barman, T. 2010, Natur, 468, 1080
Metchev, S. A., Heinze, A., Apai, D., et al. 2015, ApJ, 799, 154
Metchev, S. A., & Hillenbrand, L. A. 2006, ApJ, 651, 1166
Miles-Páez, P. A., Metchev, S., Apai, D., et al. 2019, ApJ, 883, 181
Miles-Páez, P. A., Metchev, S., Luhman, K. L., Marengo, M., & Hulsebus, A. 2017, AJ, 154, 262
Moore, K., Scholz, A., & Jayawardhana, R. 2019, ApJ, 872, 159
Morley, C. V., Marley, M. S., Fortney, J. J., & Lupu, R. 2014, ApJL, 789, L14
Naud, M.-E., Artigau, É., Rowe, J. F., et al. 2017, AJ, 154, 138
Pineda, J. S., Hallinan, G., & Kao, M. M. 2017, ApJ, 846, 75
Radigan, J., Jayawardhana, R., Lafrenière, D., et al. 2012, ApJ, 750, 105
Radigan, J., Lafrenière, D., Jayawardhana, R., & Artigau, E. 2014, ApJ, 793, 75
Reid, I. N., Cruz, K. L., Kirkpatrick, J. D., et al. 2008, AJ, 136, 1290
Riedel, A. R., Blunt, S. C., Lambrides, E. L., et al. 2017, AJ, 153, 95
Rodríguez-Ledesma, M. V., Mundt, R., Eislöffel, J., & Herbst, W. 2009, A&A, 502, 883
Scargle, J. D. 1982, ApJ, 263, 835
Schneider, A. C., Cushing, M. C., Kirkpatrick, J. D., et al. 2014, AJ, 147, 34
Schneider, A. C., Windsor, J., Cushing, M. C., & Kirkpatrick, J. D. 2017, AJ, 153, 196
Scholz, A., & Eislöffel, J. 2004, A&A, 419, 249
Scholz, A., Moore, K., Jayawardhana, R., et al. 2018, ApJ, 859, 153
Schwarz, G. 1978, AnSta, 6, 461
Shkolnik, E. L., Allers, K. N., Kraus, A. L., Liu, M. C., & Flagg, L. 2017, AJ, 154, 69
Simcoe, R. A., Burgasser, A. J., Schechter, P. L., et al. 2013, PASP, 125, 270
Tamburo, P., & Muirhead, P. S. 2019, PASP, 131, 114401
Tan, X., & Showman, A. P. 2021, MNRAS, 502, 678
Tannock, M. E., Metchev, S., Heinze, A., et al. 2021, ApJ, 161, 224
Torres, C. a. O., Quast, G. R., Melo, C. H. F., & Sterzik, M. F. 2008, in Handbook of Star Forming Regions, ed. B. Reipburth, Vol. II (San Francisco, CA: ASP)
Tremblin, P., Phillips, M. W., Emery, A., et al. 2020, A&A, 643, A23
Vos, J. M., Allers, K. N., & Biller, B. A. 2017, ApJ, 842, 78
Vos, J. M., Allers, K. N., Biller, B. A., et al. 2018, MNRAS, 474, 1041
Vos, J. M., Biller, B. A., Allers, K. N., et al. 2020, AJ, 160, 38
Vos, J. M., Biller, B. A., Allers, K. N., et al. 2020, VizieR On-line Data Catalog: J/AJ/160/38
Vos, J. M., Biller, B. A., Bonavita, M., et al. 2019, MNRAS, 483, 480
Wang, J. J., Ruffio, J.-B., Morris, E., et al. 2021, AJ, 162, 148
Wilson, P. A., Rajan, A., & Patience, J. 2014, A&A, 566, A111
Yang, H., Apai, D., Marley, M. S., et al. 2016, ApJ, 826, 8
Zhang, Z., Liu, M. C., Best, W. M. J., Dupuy, T. J., & Siverd, R. J. 2021, ApJ, 911, 7
Zhou, Y., Apai, D., Lew, B. W. P., et al. 2019, AJ, 157, 128
Zhou, Y., Apai, D., Metchev, S., et al. 2018, AJ, 155, 132
Zhou, Y., Apai, D., Schneider, G. H., Marley, M. S., & Showman, A. P. 2016, ApJ, 818, 176
Zhou, Y., Bowler, B. P., Morley, C. V., et al. 2020, AJ, 160, 77
Zuckerman, B., Bessell, M. S., Song, I., & Kim, S. 2006, ApJL, 649, L115